ENERGY TRANSFER THEORY BETWEEN ER AND SILICON NANOCRYSTAL

ENERGY TRANSFER THEORY BETWEEN ER3+ ION AND SILICON NANOCRYSTAL IN OPTICAL CAVITY AND ELECTRIC FIELD

by

QINGYI GUO, B. Sc.

OCTOBER, 2007

A Thesis

Submitted to the School of Graduate Studies

in Partial Fulfillment of the Requirements

for the Degree of

Master of Applied Science

McMaster University

© Copyright by Qingyi Guo, October 2007

MASTER OF APPLIED SCIENCE (2007)	McMaster University
(Electrical & Computer Engineering)	Hamilton, Ontario

TITLE: Energy Transfer Theory between Er3+ ion and Silicon Nanocrystal in Optical Cavity and Electric Field

AUTHOR: Qingyi Guo, B. Sc. (Peking University, China)

SUPERVISOR: Dr. Wei-Ping Huang, Professor

NUMBER OF PAGES: viii, 60

Abstract

The need for higher bandwidth and people's desire to be "always connected" have spurred a new era of silicon photonics. The traditional integrated electrical transmission lines have been an obstacle preventing ultra high speed communication. Using monolithic chips of integrated optoelectronic circuits from silicon provides an economic way to realize Tetra Byte/Second bandwidth in a variety of areas such as "fiber to the home" and the buses linking chips inside computer.

The heart of such optoelectronics—silicon laser—is still in pursuit. One of the most promising approaches is the erbium doped silicon nanocrystals embedded in silica system. External photon or hot electrons injection excites the silicon nanocrystals, which then transfer their energies to nearby erbium ions to emit light at 1.55 μm wavelength range.

In this thesis, we investigate the effects of cavity and electric field on energy transfer from Si nanocrystals (Si-nc's) to Er ions, and simulate material gain in such systems. Our results show that microcavity can enhance the Forster energy transfer and material gain, reducing the requirements for Si-nc pumping. The electric field will hinder the radiation decay of Si-nc, but we have to further explore the tunneling mechanism before concluding the overall effect of electric field. Some future work needs to be done, which will shine some light on the design of the silicon laser.

Acknowledgements

I would like to express my highest appreciation to my supervisor, Dr. Wei-Ping Huang, whose guidance, support and encouragement made this work possible to be completed. His diverse insights and pivotal ideas lead me to the frontier of photonics; from him, I have learnt the creativity and rigorousness in research.

I greatly appreciate the assistance I received from my committee members, Dr. Xun Li and Dr. Chang-Qing Xu. Their constructive criticism and valuable advice on numerical and physical modeling helped me a lot in this study. I am also very thankful to Dr. Seyed M. Sadeghi for his wholesome directions and comments throughout my work.

I would like to say many thanks to my colleagues in the Photonic Research Group for their help and friendship. They made a direct contribution in this thesis by proofreading it. I would also like to thank the administrative and technical staffs in Department of Electrical and Computer Engineering for their tireless effort and helpful attitude.

Last but not least, I would like to thank my parents, Shucheng and Kezhen, for their endless love and support in my whole life. I also want to thank my boyfriend, Haining, who not only support me morally, but also did part of the coding.

Table of Contents

Abstract ... iii

Acknowledgements ... iv

Table of Contents ... v

List of Figures ... vii

List of Tables ... viii

Chapter 1. Introduction ... 1

1.1 Background for Silicon Photonics ... 1

1.2 Si-Based Light Source ... 2

1.3 Thesis Outline ... 3

Chapter 2. Dipole Theories ... 5

2.1 Spontaneous Decay ... 5

2.1.1 Homogeneous Environment ... 5

2.1.2 Inhomogeneous Environment ... 7

2.2 Energy Transfer between Two Particles ... 8

2.3 Summary ... 15

Chapter 3. Microcavity Effect on Energy Transfer 16

3.1 Introduction 16

3.2 Material Gain 17

3.3 Simplified Model for Metal Microcavity 20

3.4 Green's Function Simulation for Multilayer 27

3.5 Summary and Future work 36

Chapter 4. Silicon Nanocrystal in Electric Field 37

4.1 Introduction 37

4.2 Variational Method 37

4.3 Band Structure of Silicon 38

4.4 Wavefunction of Si-nc in Electric Field 40

4.5 Transition Energy 43

4.6 Transition Rate 48

Chapter 5. Summary and Future work 52

References 56

List of Figures

Figure 1-1 Simplified energy diagram of Si with major recombination processes. 2

Figure 2-1 Lorentzian lineshape spectrum......... 6

Figure 2-2 The energy transfer from donor to acceptor......... 8

Figure 2-3 Si-nc and Er ions interaction......... 9

Figure 2-4 The system of two dipoles......... 10

Figure 3-1 Energy transfer diagram for Si-nc and Er coupled system. 18

Figure 3-2 A planar cavity of length L. 21

Figure 3-3 Spontaneous emission rate as a function of normalized cavity length......... 22

Figure 3-4 Er ion absorption spectra for 980 nm band. 24

Figure 3-5 Material gain for metal cavity with QY=1......... 26

Figure 3-6 Material gain for metal cavity with QY=0.5......... 26

Figure 3-7 Material gain for metal cavity with QY=0.1......... 27

Figure 3-8 Multilayer system consisting of N layers. 29

Figure 3-9 Contour deformation in complex k_ρ plane......... 33

Figure 3-10 Comparison of Bessel function along real axis and Hankel function along imaginary axis......... 34

Figure 3-11 Green's tensor in inhomogeneous medium. 35

Figure 3-12 Green's tensor in 4-layer media......... 36

Figure 4-1 Band structure of Si. The energy unit is eV. 39

Figure 4-2 Iso-energy surfaces of the holes (a) and electrons (b). 39

Figure 4-3 Electron energy as a function of variational parameter. 44

Figure 4-4 Hole energy as a function of variational parameter. 45

Figure 4-5 Variational parameters for electrons. 46

Figure 4-6 Variational parameters for holes. 46

Figure 4-7 Transition energy for different size of Si-nc's in electric field. 47

Figure 4-8 Radiation rate for direct transitions. 49

Figure 4-9 Radiation rate for phonon-assisted transitions. 51

Figure 5-1 Random distribution of Si- nc's in SiO_2 matrix. 53

Figure 5-2 Forster energy transfer between different Si-nc's. 53

Figure 5-3 Random distribution of Si-nc's and Er. 54

Figure 5-4 Inhomogeneous broadening of Si-nc's 54

List of Tables

Table 1 Parameters in rate equations 18

Chapter 1.

Introduction

1.1 Background for Silicon Photonics

High speed communication is always what people desire [1][2]. For the flow of information, each component in the loop has to provide a broad band in order to achieve the fast performance when all comes to all. Since the invention of optical fiber and EDFA, the long-haul data transmission link advances to GHz regime. Experts in micro-electronics nowadays can build up computer chips with over one billion transistors per square centimeter in pursuit of Moore's Law. The multi-core processors are booming, too. Thus, the processing capacity is heading 14 GHz by 2009 [3]. However, the traditional integrated electrical transmission lines for connecting these nano-transistors to the other chips or the optical link has been a bottleneck. This has been a limiting factor in chip-speed performance not following up Moore's Law.

The dielectric optical waveguide interconnect is an ideal replacement for the metallic interconnect, providing dense line packing and high frequency operation. Unfortunately, today, optical devices are bulky, assembled from discrete components, and mostly fabricated from expensive III-V compound semiconductors. Using monolithic chips of integrated optoelectronic circuits from silicon not only saves the cost of raw material, but also utilizes the VLSI fabrication infrastructure. It provides an economic

way to realize Tetra Byte/Second bandwidth in a variety of areas such as "fiber to the home" and the buses linking chips inside computer.

The realization of monolithic Si photonics requires the development of four kinds of devices: a) light source and amplifier; b) modulator and optical switches; c) passive waveguides, including the guiding, coupling, splitting and combining of light; d) photo detector. The last three categories of components have been demonstrated in Si-based materials, but the heart of such optoelectronics—silicon laser—is still in pursuit.

1.2 Si-Based Light Source

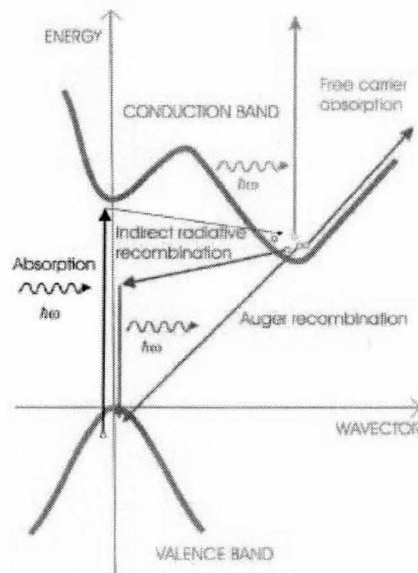

Figure 1-1 Simplified energy diagram of Si with major recombination processes. [1].

The in-direct bandgap of Si is the fundamental limitation for the light source. The electron-hole radiative recombination time is of the order of milliseconds, since it is a

second-order process (phonon involved). However, the nonradiative lifetime is nanosecond, giving the Si internal quantum efficiency of 1 in a million. Besides, Auger recombination and free carrier absorption, shown in Figure 1-1, also limit the use of Si as light source or amplifier.

To overcome the natural limitation of Si, people explored several approaches, some of which are impressive: a) For bulk Si, people make it ultra-pure with careful surface passivation and texturing [4], or introduce implant-induced dislocation loops [5]. In these ways they eliminate non-radiative defects or decrease the free carrier diffusion length. b) SiGe alloy systems can be engineered to have more direct-like bandgap, enhancing the quantum efficiency (see for example, [6]). c) Use low-dimension material, e.g. porous Si or Si nanocrystals (Si-nc's) [7], to confine electron and hole with wavefunction overlap. d) Introduce impurity luminescence centers, such as rare-earth doping of Si-nc in silica [8]. e) Other approaches, including the continuous-wave silicon laser using stimulated Raman scattering [9], and the electrically driven InP and Si hybrid laser [10] released by Intel Corporation.

1.3 Thesis Outline

In this thesis, we focus on the erbium (Er) doped Si-nc embedded in SiO_2. We aim to theoretically investigate the effects of cavity and electric field on energy transfer from Si-nc's to Er ions, calculate the gain in such systems, hoping to shine some light on design of optical devices based on the results of these studies.

The outline is as follows. In Chapter 2, we will explore the general dipole theories of spontaneous decay and energy transfer between two particles using semi-classical approach. It shows that Green's function is a proper and convenient description for cavity effect on the energy transfer from Si-nc to Er ion. In Chapter 3, we will first use a simplified energy transfer model to describe a metal microcavity. The primitive estimation will show that microcavity could lead to significant improvements, enhancing the Forster energy transfer and material gain while reducing the requirements of optical pumping. We will then discuss the numerical accurate simulation of Green's tensor in multilayer system. In Chapter 4, we will give a brief background for variational method and the bandgap properties of silicon. Based on that, we will calculate the electric field effect on the silicon transition energy and rate using a quantum dot model for Si-nc. There we study both the "quasi"-direct transition and the phonon-assisted transition. And finally, we will give the summary and plan for future work in Chapter 5.

Chapter 2.

Dipole Theories

2.1 Spontaneous Decay

2.1.1 Homogeneous Environment

A widely accepted classical approach to deal with spontaneous decay is to consider a harmonically oscillating dipole [11]. Throughout the thesis, we assume time harmonic fields with an $\exp(-i\omega t)$ convention. In homogeneous environment, the equation of motion for an undriven harmonically oscillating dipole is

$$\frac{d^2}{dt^2}\boldsymbol{\mu}(t)+\gamma_0\frac{d}{dt}\boldsymbol{\mu}(t)+\omega_0^2\boldsymbol{\mu}(t)=0 \tag{2.1}$$

where $\boldsymbol{\mu}(t)$ is the dipole moment. For a distribution of charges q_n with coordinates $\mathbf{r}_n$ and origin $\mathbf{r}_0$, the dipole moment is defined by

$$\boldsymbol{\mu}(t)=\sum_n q_n\left[\mathbf{r}_n(t)-\mathbf{r}_0\right] \tag{2.2}$$

The natural frequency of the oscillator is ω_0, and its decay rate is γ_0. The lifetime τ_0 is the time for which the energy decays to 1/e of its initial value at t = 0.

$$\tau_0=1/\gamma_0 \tag{2.3}$$

The intrinsic quantum yield q_i is defined by

$$q_i = \frac{\gamma_r}{\gamma_r + \gamma_{nr}} \tag{2.4}$$

where γ_r and γ_{nr} are the radiative and non-radiative decay rates, respectively. For a dipole with charge q and mass m, the radiative decay rate can be expressed as

$$\gamma_0 = q_i \frac{1}{4\pi\varepsilon_0} \frac{2q^2\omega_0^2}{3mc^3} \tag{2.5}$$

The total energy per unit solid angle $d\Omega$ per unit frequency interval $d\omega$ can be expressed as

$$\frac{dW}{d\Omega d\omega} = \frac{1}{4\pi\varepsilon_0} \frac{|\mathbf{\mu}|^2 \sin^2\theta\omega_0^2}{4\pi^2c^3\gamma_0^2} \left[\frac{\gamma_0^2/4}{(\omega-\omega_0)^2 + \gamma_0^2/4} \right] \tag{2.6}$$

where θ is the azimuth coordinate in the spherical coordinates. The expression in the brackets determines the spectral shape, known as the Lorentzian lineshape function [Figure 2-1]. The width at half its maximum height is $\Delta\omega = \gamma_0$, called radiative linewidth.

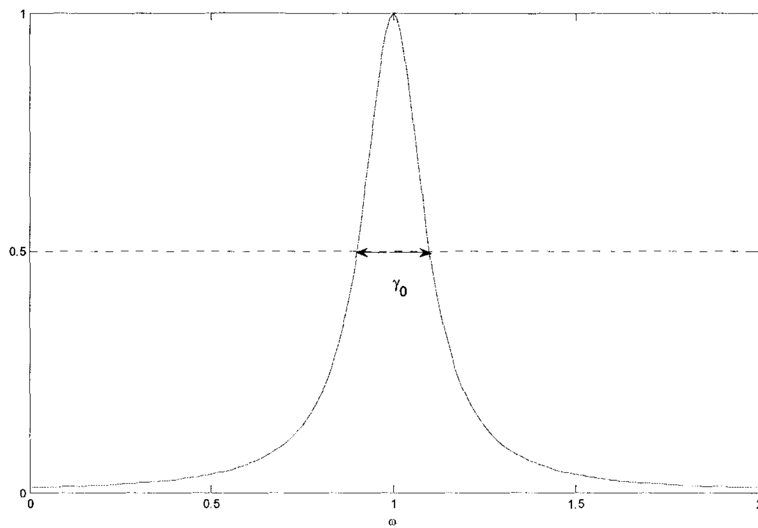

Figure 2-1 Lorentzian lineshape spectrum

2.1.2 Inhomogeneous Environment

In an inhomogeneous environment, the dipole's own field emitted at a former time will come back to dipole's position after it has been scattered in the environment. This is called the secondary field $\mathbf{E}_s(t)$ of the dipole, and is the driving force for the oscillating dipole. The equation of motion is

$$\frac{d^2}{dt^2}\boldsymbol{\mu}(t)+\gamma_0\frac{d}{dt}\boldsymbol{\mu}(t)+\omega_0^2\boldsymbol{\mu}(t)=\frac{q^2}{m}\mathbf{E}_s(t) \tag{2.7}$$

The solution is in the form

$$\boldsymbol{\mu}(t)=\mathrm{Re}\left\{\boldsymbol{\mu}_0 e^{-i\omega t}e^{-\gamma t/2}\right\},\quad \mathbf{E}_s(t)=\mathrm{Re}\left\{\mathbf{E}_0 e^{-i\omega t}e^{-\gamma t/2}\right\} \tag{2.8}$$

where γ and ω are the new decay rate and resonance frequency, respectively. After some evaluations, we obtain the modification of the normalized decay rate

$$\frac{\gamma}{\gamma_0}=1+q_i\frac{6\pi\varepsilon_0}{|\boldsymbol{\mu}_0|^2}\frac{1}{k^3}\mathrm{Im}\left\{\boldsymbol{\mu}_0^*\cdot\mathbf{E}_s(\mathbf{r}_0)\right\} \tag{2.9}$$

The inhomogeneous environment will also induce a frequency shift $\Delta\omega=\omega-\omega_0$, written as

$$\frac{\Delta\omega}{\gamma_0}=q_i\frac{3\pi\varepsilon_0}{|\boldsymbol{\mu}_0|^2}\frac{1}{k^3}\mathrm{Re}\left\{\boldsymbol{\mu}_0^*\cdot\mathbf{E}_s(\mathbf{r}_0)\right\} \tag{2.10}$$

If we look at the Poynting's vector, the normalized rate of energy dissipation is

$$\frac{P}{P_0}=1+\frac{6\pi\varepsilon_0}{|\boldsymbol{\mu}_0|^2}\frac{1}{k^3}\mathrm{Im}\left\{\boldsymbol{\mu}_0^*\cdot\mathbf{E}_s(\mathbf{r}_0)\right\} \tag{2.11}$$

where P denotes power. Comparing with Eq. (2.9), we get

$$\frac{\gamma}{\gamma_0} = q_i \frac{P}{P_0} + 1 - q_i \tag{2.12}$$

If internal quantum yield is equal to 1, we can get

$$\frac{\gamma}{\gamma_0} = \frac{P}{P_0} \tag{2.13}$$

2.2 Energy Transfer between Two Particles

Two particles, each having a set of discrete energy levels, are coupled if a) they are close to each other and b) their energy levels overlap. In this case, one particle pumped to its excited state may give up its energy, and decay to its ground state. The other particle accepts this transition energy, is pumped to the excited level, and then decays. We denote them as **D** (donor) and **A** (acceptor). [Figure 2-2] In our system of silicon nanocrystal (Si-nc) and erbium (Er) ion, Si-nc absorbs external energy (optical pumping or hot electron) much more efficiently than Er ion. If Si-nc is energy resonant with Er, energy will be transferred from Si-nc (donor) to Er (acceptor).

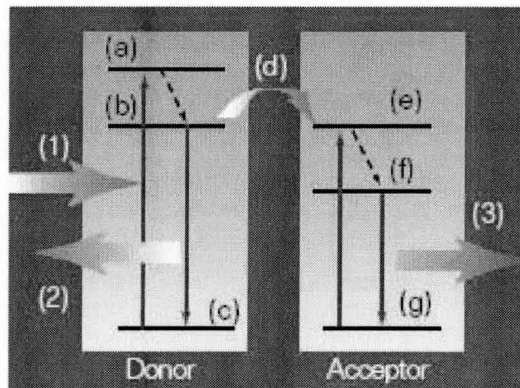

Figure 2-2 The energy transfer from donor to acceptor.

There are two kinds of energy transfers. a) If these two particles are relatively far to each other, the donor decays and generate one photon. Then the photon travels to the site of acceptor, and gets absorbed. This process is very inefficient. [Figure 2-3 (a)] b) If two particles are spaced closely, the transition energy will be non-radiatively transferred to the acceptor. There is no photon involved, thus this process is fast and efficient. [Figure 2-3 (b)] We will confine ourselves to the second kind of energy transfer.

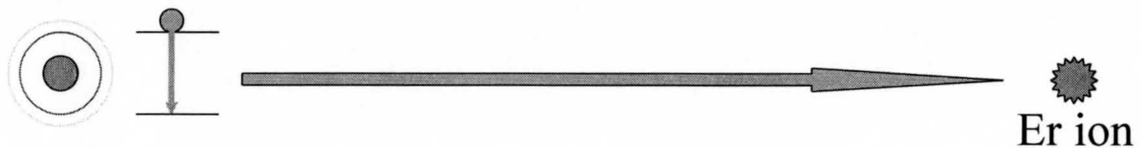

(a) Si-nc and Er ion are far from each other (>>1.5 μm)

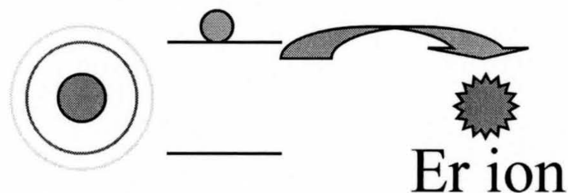

(b) Si-nc and Er ions are very close (<<1.5 μm)

Figure 2-3 Si-nc and Er ions interaction

We use the semi-classical framework to describe the energy transfer [11]. This is a self-consistent approach. It matches the empirical formula from experiments, and yet provides some freedom to play with different medium settings. It generates the same form of formulas with quantum electrodynamic theory, and is relatively easier to understand.

Assume the donor to be a dipole radiating at frequency ω_0, and the acceptor to be an absorber at ω_0. Both particles are embedded in a medium with refractive index $n(\omega)$. The transition dipole moments of donor and acceptor are denoted as $\boldsymbol{\mu}_D$ and $\boldsymbol{\mu}_A$, respectively. The corresponding units are $\mathbf{n}_D$ and $\mathbf{n}_A$. The positions of donor and acceptor are $\mathbf{r}_D$ and $\mathbf{r}_A$, respectively. $\mathbf{R} = \mathbf{r}_A - \mathbf{r}_D$ is the vector from donor to acceptor, with the corresponding unit $\mathbf{n}_R$. This is shown in Figure 2-4.

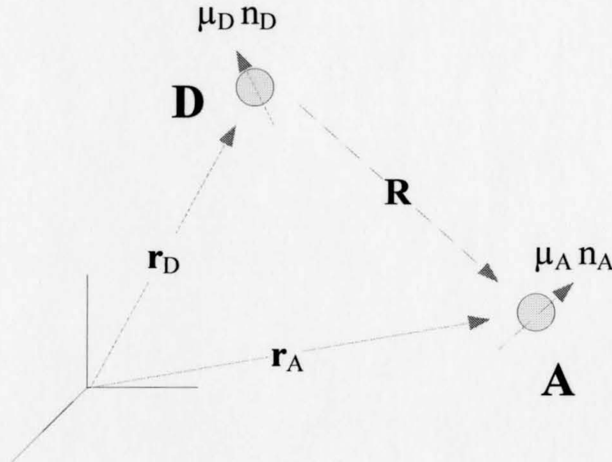

Figure 2-4 The system of two dipoles.

We start from Eq. (2.12), which connects the quantum mechanical picture with the classical picture, written as

$$\frac{\gamma_{D\to A}}{\gamma_0} = q_i \frac{P_{D\to A}}{P_0} + 1 - q_i \tag{2.14}$$

where $\gamma_{D\to A}$ is the energy transfer rate from donor to acceptor, and γ_0 is the donor's radiative decay rate in the absence of the acceptor in homogeneous medium. $P_{D\to A}$ is the

donor's energy absorbed by the acceptor per unit time, and P_0 is the energy released from the donor per unit time in the absence of the acceptor. P_0 can be expressed as

$$P_0 = \frac{|\boldsymbol{\mu}_D|^2 n(\omega_0)}{12\pi\varepsilon_0 c^3}\omega_0^4 \tag{2.15}$$

which is the well known result for dipole in homogeneous medium. We are interested in the normalized transfer rate involving inhomogeneous environment and the donor, $\frac{\gamma_{D\to A}}{\gamma_0}$, therefore we only need to calculate $P_{D\to A}$.

$P_{D\to A}$ can be written according to Poynting's theorem

$$P_{D\to A} = -\frac{1}{2}\int_{V_A} \mathrm{Re}\{\mathbf{j}_A^* \cdot \mathbf{E}_D\} dV \tag{2.16}$$

where $\mathbf{j}_A$ is the current density of the acceptor, and $\mathbf{E}_D$ is the electric field generated by the donor. Here we adopt the dipole approximation

$$\mathbf{j}_A = -i\omega_0 \boldsymbol{\mu}_A \delta(\mathbf{r} - \mathbf{r}_A) \tag{2.17}$$

Thus Eq. (2.17) reduces to

$$P_{D\to A} = \frac{\omega_0}{2}\mathrm{Im}\{\boldsymbol{\mu}_A^* \cdot \mathbf{E}_D(\mathbf{r}_A)\} \tag{2.18}$$

Note that $\boldsymbol{\mu}_A$ is not a permanent dipole moment, but it is a transition moment induced by the donor's field. In the linear regime we have

$$\boldsymbol{\mu}_A = \overleftrightarrow{\alpha}_A \mathbf{E}_D(\mathbf{r}_A) \tag{2.19}$$

where $\overleftrightarrow{\alpha}_A$ is the acceptor's polarizability tensor. It can be expressed in terms of the absorption cross-section σ

$$\sigma(\omega_0) = \frac{\langle P(\omega_0) \rangle}{I(\omega_0)} \tag{2.20}$$

where $\langle P \rangle$ is the power absorbed by the acceptor averaged over all possible dipole orientations, and I is the incident intensity. Then we can get

$$P_{D \to A} = \frac{3}{2}\sqrt{\frac{\varepsilon_0}{\mu_0}} n(\omega_0)\sigma_A(\omega_0)\left|\mathbf{n}_A \cdot \mathbf{E}_D(\mathbf{r}_A)\right|^2 \tag{2.21}$$

The donor's field at the position of acceptor $\mathbf{E}_D(\mathbf{r}_A)$ can be expressed in terms of the Green's function $\overleftrightarrow{\mathbf{G}}$ (in any medium, say, a microcavity) as

$$\mathbf{E}_D(\mathbf{r}_A) = \omega_0^2 \mu \overleftrightarrow{\mathbf{G}}(\mathbf{r}_D, \mathbf{r}_A) \cdot \boldsymbol{\mu}_D \tag{2.22}$$

where $\mu = \mu_0 \mu_r$ is the permeability. After some derivation we can get the normalized transferred power from donor to acceptor

$$\frac{P_{D \to A}}{P_0} = \frac{9c^4}{8\pi R^6} \frac{\sigma_A(\omega_0)}{n^4(\omega_0)\omega_0^4} T(\omega_0) \tag{2.23}$$

where the function

$$T(\omega_0) = 16\pi^2 k^4 R^6 \left|\mathbf{n}_A \cdot \overleftrightarrow{\mathbf{G}}(\mathbf{r}_D, \mathbf{r}_A) \cdot \mathbf{n}_D\right|^2 \tag{2.24}$$

and $R = |\mathbf{R}|$ is the distance between donor and acceptor.

Eq. (2.23) can be rewritten in terms of delta function as

$$\frac{P_{D \to A}}{P_0} = \frac{9c^4}{8\pi R^6} \int_0^\infty \frac{\delta(\omega - \omega_0)\sigma_A(\omega)}{n^4(\omega)\omega^4} T(\omega) d\omega \tag{2.25}$$

where $\delta(\omega-\omega_0)$ can be regarded as spectrum of donor emission. For real atoms or clusters, dipole emits over a range of frequencies. We use $f_D(\omega)$ to denote the donor's normalized emission spectrum in the medium

$$\int_0^\infty f_D(\omega)d\omega = 1 \tag{2.26}$$

and generalize Eq. (2.25) to

$$\frac{P_{D\to A}}{P_0} = \frac{9c^4}{8\pi R^6}\int_0^\infty \frac{f_D(\omega)\sigma_A(\omega)}{n^4(\omega)\omega^4}T(\omega)d\omega \tag{2.27}$$

There are several important points to note:

a) In free space, at short distances, $T(\omega)$ is constant and the transfer rate decays as $1/R^6$. For intermediate distances, $T(\omega)$ scales as R^2, and the transfer rate decays as $1/R^4$. For large distances, $T(\omega)$ scales as R^4, and the transfer rate decays as $1/R^2$. The transfer rate decreases rapidly if the distance between donor and acceptor increases. We only consider Forster energy transfer rate in near field, where $R << 1/k, k = 2\pi n(\omega)/\lambda$. In this case, the normalized transfer rate is proportional to $1/R^6$, and $T(\omega)$ is normally denoted as κ^2, the orientation factor. Then the energy transfer can be expressed as

$$\frac{P_{D\to A}}{P_0} = \left[\frac{R_0}{R}\right]^6, \quad R_0^6 = \frac{9c^4}{8\pi}\int_0^\infty \frac{f_D(\omega)\sigma_A(\omega)\kappa^2(\omega)}{n^4(\omega)\omega^4}d\omega \tag{2.28}$$

where R_0 is a characteristic distance for a given system.

b) The normalized transfer rate depends on the spectral overlap of the donor's emission spectrum f_D and the acceptor's absorption cross-section. This is the energy resonant condition.

c) In inhomogeneous environment, e.g. a microcavity, the donor's emission spectrum f_D will be changed, and the weighting function $T(\omega)$ will also change according to the Green function in this circumstance. To obtain the quantitively exact transfer rate, we have to calculate the Green function as the first step. From Eqs. (2.9) and (2.10), we can get the modified donor's emission spectrum f_D. From Eqs. (2.14), (2.24) and (2.28), we can obtain the final transfer rate.

In the biochemical area, people usually deal with molecules in solutions [12]. We can regard this as a homogeneous system. Inserting the free space Green's function into Eq. (2.24), we can get for the near field

$$\kappa^2 = [\mathbf{n}_A \bullet \mathbf{n}_D - 3(\mathbf{n}_R \bullet \mathbf{n}_D)(\mathbf{n}_R \bullet \mathbf{n}_A)]^2 \tag{2.29}$$

κ^2 has a value in the range of [0,4]. The relative orientation of donor and acceptor is often unknown; therefore the orientational average is adopted.

$$\langle \kappa^2 \rangle = \frac{2}{3} \tag{2.30}$$

Also, they consider $q_i = 1$, and the energy transfer is in the form of

$$\gamma_{transfer} = \gamma_{Donor} \left(\frac{R_0}{R} \right)^6 \tag{2.31}$$

This enhancement of Foster energy transfer rate leads to suppression of the donor transition, while efficiently increasing the acceptor emission.

2.3 Summary

In this chapter we analyze the theoretical expressions of spontaneous decay of a dipole, and further the Forster energy transfer rate between two dipoles. The formulas developed here are general, thus are the simulation starting points. We will use them to evaluate the microcavity effect and electric field effect on our Er doped Si-nc system.

Chapter 3.

Microcavity Effect on Energy Transfer

3.1 Introduction

A laser is based on three critical components (see, for example, [13]). First, we must have the active material which is able to generate and amplify light via stimulated emission of photons, called gain material. Second, an optical cavity provides the optical feedback to convert an amplifier into an oscillator. Third, a pumping mechanism excites the active material such that population inversion is achieved.

There are a lot of optical cavities in practical design. Some of the typical ones are: a) Fabry-Perot (FP) cavity, formed by two simple mirrors at the ends. b) Bragg cavity, composed by two Bragg reflectors at the ends [14][15]. The fabrication is compatible with the semiconductor infrastructure, and well controlled. In our case, we can simply use 4 or 5 pairs of Si and SiO_2 layers due to the strong index contrast. c) Slot waveguide, where light is strongly confined in the low-index material [16][17]. It gives rise to a strong electric field amplitude, thus the highly efficient interaction between fields and active materials. It also provides a possibility to the electrical pumping of our Er doped Si-nc system. d) Other cavities, e.g. micro-ring [17], photonic crystal [18].

In this chapter, we discuss the 1D optical cavity effect with optical pumping.

3.2 Material Gain

Pacifici et al. [19] conduct a detailed study of the optical properties for the Er-doped Si nanocrystals system. They present a phenomenological model using a set of coupled first order differential rate equations to describe the time evolution of the population for both the Si-nc and the Er related excited levels. In their model, they consider five energy levels for Er, and two energy levels for Si-nc. Not only the strong coupling between each Si-nc and the neighboring Er ions is accounted, the interactions between pairs of Er ions are also included, such as the concentration quenching effect and the cooperative up-conversion mechanism. They study the steady state and time resolved luminescence signals at both the 1.54 and 0.98 μm Er lines and at the Si-nc emission lines (around 0.8 μm). Their model fits well with experiments' results.

We can use a simplified Er energy model including only three energy levels [20] if we neglect the high-order process, and note a) there is no photoluminescence (PL) line from energy levels higher than 980 nm observed, b) the exciton emission from Si-nc's generally overlaps the 980 nm absorption band, and c) energy transfer from Si-nc to Er can occur via the $^4I_{11/2}$ energy level. The energy diagram for the Si-nc and Er system is shown in Figure 3-1.

The parameters used are listed in Table 1 below. They are adapted from either experiments, or experimental fitting of simulation models.

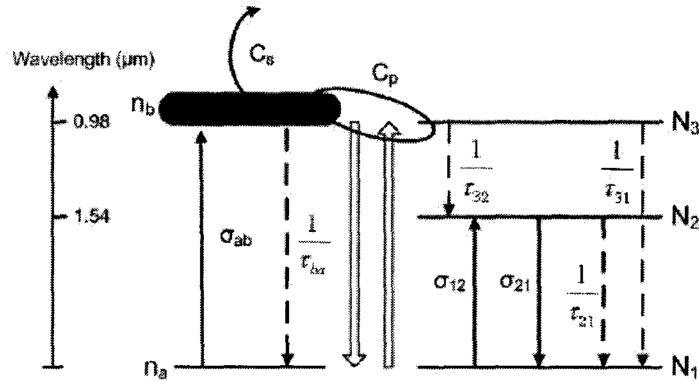

Figure 3-1 Energy transfer diagram for Si-nc and Er coupled system.

Table 1 Parameters in rate equations [20].

Notation	Physical Meaning	Typical Value
N_T	Er doping concentration	3e19 [cm^{-3}]
n_T	Si-nc concentration	3e19 [cm^{-3}]
σ_{ab}	Si-nc excitation cross-section	5e-17 [cm^{2}]
σ_{21}	Signal emission cross-section	6e-20 [cm^{2}]
σ_{12}	Signal absorption cross-section	6e-20 [cm^{2}]
C_p	Si-nc / Er coupling	7e-16 [cm^{3}s^{-1}]
C_s	Free electron absorption	3e-19 [cm^{3}s^{-1}]
τ_{ab}	Lifetime ($b \to a$)	2.5e-5 [s]
τ_{32}	Lifetime ($3 \to 2$)	2.4e-6 [s]
τ_{31}	Lifetime ($3 \to 1$)	7.1e-4 [s]
τ_{21}	Lifetime ($2 \to 1$)	8.5e-3 [s]

We can get the rate equations written as below

Si-nc:

$$\frac{dn_b}{dt} = \frac{\sigma_{ab} I_p^{eff}}{h\nu_p} n_a - \frac{n_b}{\tau_{ab}} - C_p n_b N_1$$

$$\frac{dn_a}{dt} = -\frac{\sigma_{ab} I_p^{eff}}{h\nu_p} n_a + \frac{n_b}{\tau_{ab}} + C_p n_b N_1$$

$$n_T = n_a + n_b$$

Er ion:

$$\frac{dN_3}{dt} = C_p n_b N_1 - \frac{N_3}{\tau_{32}} - \frac{N_3}{\tau_{31}}$$

$$\frac{dN_2}{dt} = \frac{N_3}{\tau_{32}} - \frac{N_2}{\tau_{21}} - \left(\sigma_{21} N_2 - \sigma_{12} N_1\right) \frac{I_s^{eff}}{h\nu_s} - C_s n_b N_2$$

$$\frac{dN_1}{dt} = -C_p n_b N_1 + \frac{N_2}{\tau_{21}} + \frac{N_3}{\tau_{31}} + \left(\sigma_{21} N_2 - \sigma_{12} N_1\right) \frac{I_s^{eff}}{h\nu_s} + C_s n_b N_2$$

$$N_T = N_1 + N_2 + N_3 \tag{3.1}$$

Here, h is Planck constant; $N_i\,(i = 1,2,3)$ is the Er ion density on i-th energy level; n_a, n_b are Si-nc densities on the ground and the excited state, respectively. I_p^{eff} is the effective pump intensity; ν_p is the pump frequency, which is set to be 488 nm. I_s^{eff} is the effective signal intensity, and ν_s is the signal frequency, around 1550 nm.

At this stage we concentrate on the material gain of the Si-nc and Er system. Thus we can assume the signal intensity is very weak, $I_s^{eff} \simeq 0$. We solve the time-dependent Eq. (3.1) until the density for each energy level reaches its steady state. The material gain g can be calculated by [19]

$$g = \sigma_e \left(N_2 - N_1\right) \tag{3.2}$$

where σ_e is the emission cross section of level $^4I_{13/2}$, and $(N_2 - N_1)$ is the total concentration of Er ions inverted in that level. A commonly used value $\sigma_e = 1\times10^{-19} cm^2$ is adopted here.

The coupling coefficient between Si-nc and Er ion C_p is generally considered to be a constant in literatures. However, from our analysis in Chapter 2, we can see that C_p is proportional to the energy transfer rate $\gamma_{D\rightarrow A}$. Therefore, C_p will definitely change according to different optical environment or electric field. That is to say, we can apply different optical or electrical settings to manipulate material gain, which is something novel. If C_p increases, there is a big probability that the material gain will increase, too. Starting from the material gain, we should be able to simulate the waveguide gain for a given structure, although it is more difficult to deal with the coupling between wave propagation and material gain.

3.3 Simplified Model for Metal Microcavity

For the sake of illustration, we consider a simplified model for the energy transfer rate, and the simplest microcavity formed by metal.

Several authors dealt with the spontaneous emission rate in metal microcavity, and we follow the approach by Gunnar Bjork [21]. He considers the configuration in Figure 3-2, and only considers the case when the dipole moment is equally distributed in the x and y direction. The cavity is formed by a mirror with reflectivity R_1 and R_2 on the

left and right side. Assume the mirrors extend to infinity in the xy-plane, and are ideal and lossless. That is, the mirror reflectivity and the reflection phase are fixed at R and π, respectively, for all frequencies and angles of incidence.

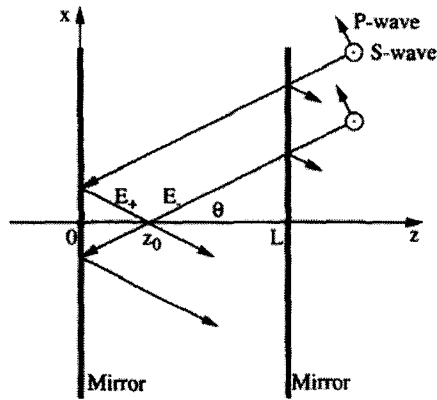

Figure 3-2 A planar cavity of length L.

From Fermi's golden rule and the calculation of mode function inside the cavity, we can get the total emission rate. For simplicity we focus on the symmetric ($R_1 = R_2 = R$) cavity, and put the dipole sheet at the center. Assume that the linewidth of the dipole matrix element is much narrower than the width of the cavity resonance, the total spontaneous emission rate Γ_{sp} can be expressed by

$$\Gamma_{sp} = \frac{3\Gamma_{sp0}}{4} \int_0^{kL} \frac{dt}{kL} \frac{(1-R)\left[1+R-2\sqrt{R}\cos t\right]}{(1-R)^2 + 4R\sin^2 t} \left[1+\left(\frac{t}{kL}\right)^2\right] \quad (3.3)$$

where Γ_{sp0} is the total emission rate in homogeneous medium, k is the wave number, and L is the cavity length. In the single mode cavity, when $R=1$, it can be written as

$$\Gamma_{sp} = \frac{3\Gamma_{sp0}}{4}\frac{2\pi}{kL}\left[1+\left(\frac{\pi}{kL}\right)^2\right] \tag{3.4}$$

Now we can evaluate normalized emission rate $\Gamma_{sp} / \Gamma_{sp0}$ as a function of the normalized cavity length L/λ for several metal cavities with $R = 0.9, 0.95, 0.99, 1$, shown in Figure 3-3. The trivial case of $R = 0$ (free space) is also plotted.

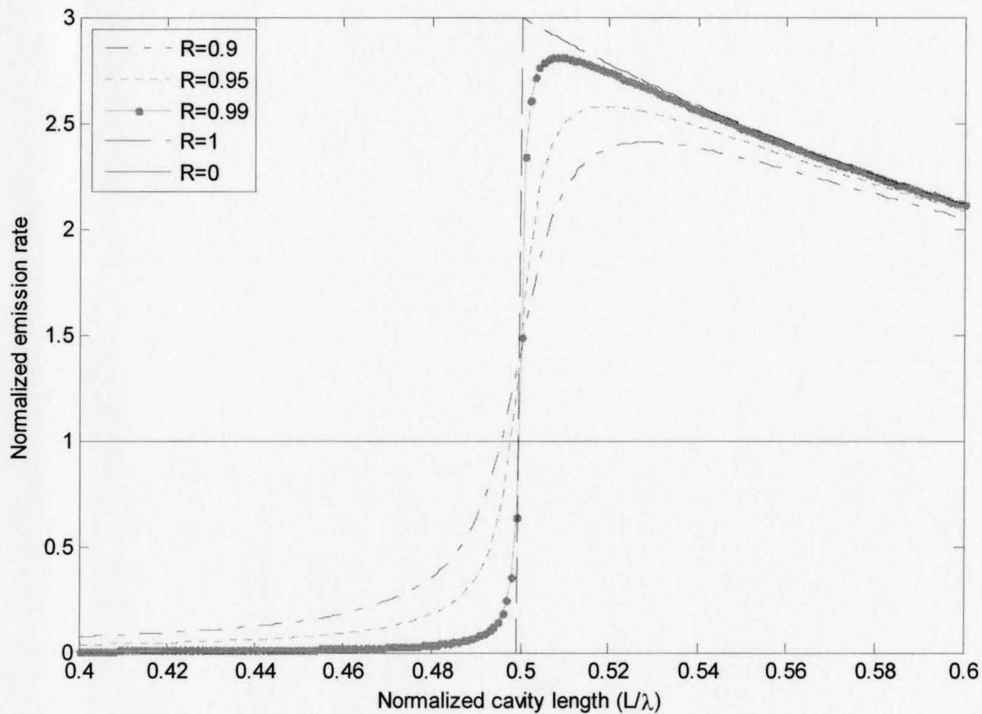

Figure 3-3 Spontaneous emission rate as a function of normalized cavity length.

We can easily see from Figure 3-3 that for a 1D metal microcavity, the maximum enhancement of emission rate is 3, with the perfect conducting metal wall. For 2D or 3D microcavity, like Photonic Crystal, or micro-ring resonator, this enhancement can be much greater.

We adopt the energy transfer formula commonly used in chemistry or biochemistry [12]. The rate of Forster energy transfer between a single donor molecule and a single acceptor is given by

$$\gamma_{tr} = \gamma_D \left(\frac{R_0}{R} \right)^6 \quad (3.5)$$

where γ_D is the donor transition rate, including the radiative decay rate γ_{Dr} and the nonradiative rate γ_{Dn}. We have $\gamma_D = \gamma_{Dr} + \gamma_{Dn}$. R is the distance between donor and acceptor, and R_0 is the critical distance defined by

$$R_0^6 = \frac{9000(\ln 10)\kappa^2 q_{iD}}{128\pi^6 n^4 N} Z \quad (3.6)$$

where κ is the orientational factor, $q_{iD} = \frac{\gamma_{Dr}}{\gamma_{Dr} + \gamma_{Dn}}$ is the donor quantum yield, n is the refractive index of the medium, N is Avogadro's number. Z is the overlap factor between the normalized emission spectrum of the donor $f_D(\nu)$ and the molar absorption spectrum of the acceptor $\sigma_A(\nu)$, given by

$$Z = \int_0^\infty f_D(\nu) \sigma_A(\nu) \frac{d\nu}{\nu^4} \quad (3.7)$$

Now we only consider one size of Si-nc and the corresponding homogeneous broadening. The linewidth of its emission spectrum is very narrow. We adopt the value in Table 1, $\tau_{ab} = 2.5 \times 10^{-5} s$, and assume quantum yield is 1. The radiative decay rate is $\gamma_{Dr} = 1/\tau_{ab} = 4 \times 10^4 s^{-1}$. Using the Lorentzian function for the lineshape, from the uncertainty principle, the linewidth of Si-nc is on the order of $10^{-8} nm$. The Er emission

cross section is shown in Figure 3-4.We can read the experimental data from [22], and fit them with four Gaussian functions. The linewidth of Er emission cross section is around 20 nm, which is much broader than the emission linewidth of Si-nc.

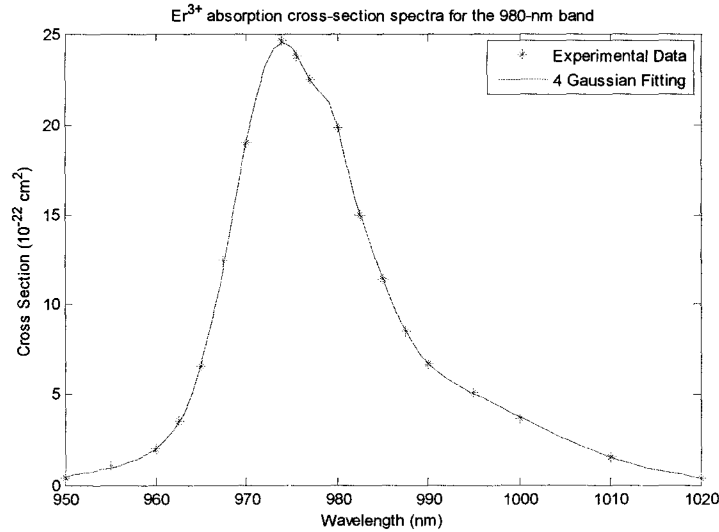

Figure 3-4 Er ion absorption spectra for 980 nm band.

Thus we make a reasonable assumption: the overlap integral Z will not change with cavity. The Si-nc radiative emission rate γ_{Dr}^{new} is enhanced by C times

$$\gamma_{Dr}^{new} = C\gamma_{Dr} \tag{3.8}$$

The nonradiative emission rate of Si-nc will not change with cavity,

$$\gamma_{Dn}^{new} = \gamma_{Dn} \tag{3.9}$$

The total transition lifetime of Si-nc is given by

$$\tau_{ab}^{new} = \frac{1}{\gamma_D^{new}} = \frac{1}{\gamma_{Dr}^{new} + \gamma_{Dn}^{new}} \tag{3.10}$$

Assume the coupling coefficient $C_p^0 = 7\times10^{-16}$ is the value for the case $\gamma_{Dr} = 4\times10^4 s^{-1}$ and a specific distance r_0. The actual distance between donor and acceptor is $R = dist * r_0$. The modified coupling coefficient in cavity is:

$$C_p^{new} \propto \gamma_D^{new}\left(\frac{R_0}{R}\right)^6 \tag{3.11}$$

and is given by

$$C_p^{new} = C\left(\frac{1}{dist}\right)^6 C_p^0 \tag{3.12}$$

The quantum yield (QY) of Si-nc can vary from 0 to 1, and can be measured from experiment (see, for example, [23]). Here we keep the Si-nc radiative emission rate γ_{Dn} as a constant, and vary the QY. The material gain can be plotted as a function of pumping intensity. If we vary $dist$, the gain will change greatly, too. In the following figures, we use the 1D ideal metal cavity, thus the amplification $C = 3$.

Figure 3-5 shows the results for QY = 1. The cavity enhancement of the donor transition rate γ_D leads to a linear increase of the transfer rate γ_{tr}, therefore the ratio between the emission intensities of the donor and the acceptor is hardly influenced. Namely, the energy-transfer and material gain cannot be increased through this setting.

We can also obtain the material gain for QY = 0.5 (Figure 3-6) and 0.1 (Figure 3-7). For QY = 0.1, the critical pumping intensity for gain is around 18 W/cm^2 without cavity, and reduced to around 8 W/cm^2 in our 1D cavity. We can see that even for this simple 1D metal cavity where light is loosely confined, the requirement of optical pumping to achieve gain is greatly reduced.

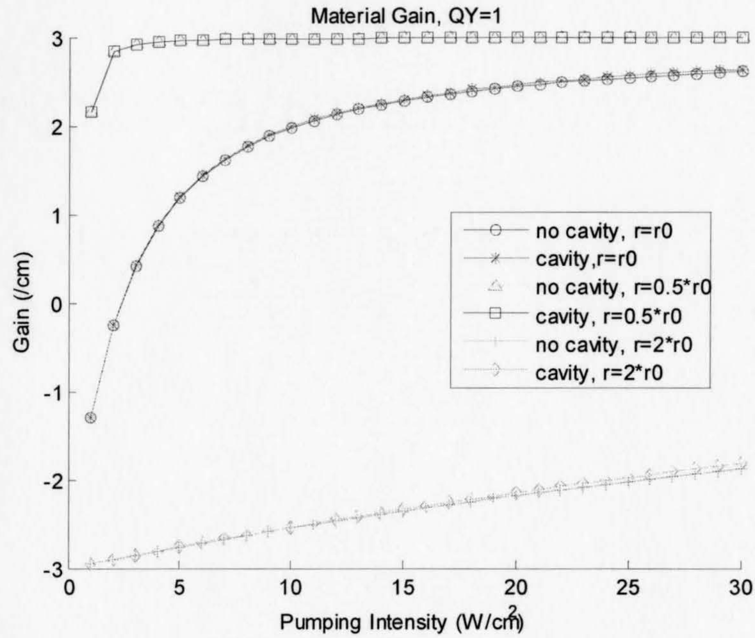

Figure 3-5 Material gain for metal cavity with QY=1.

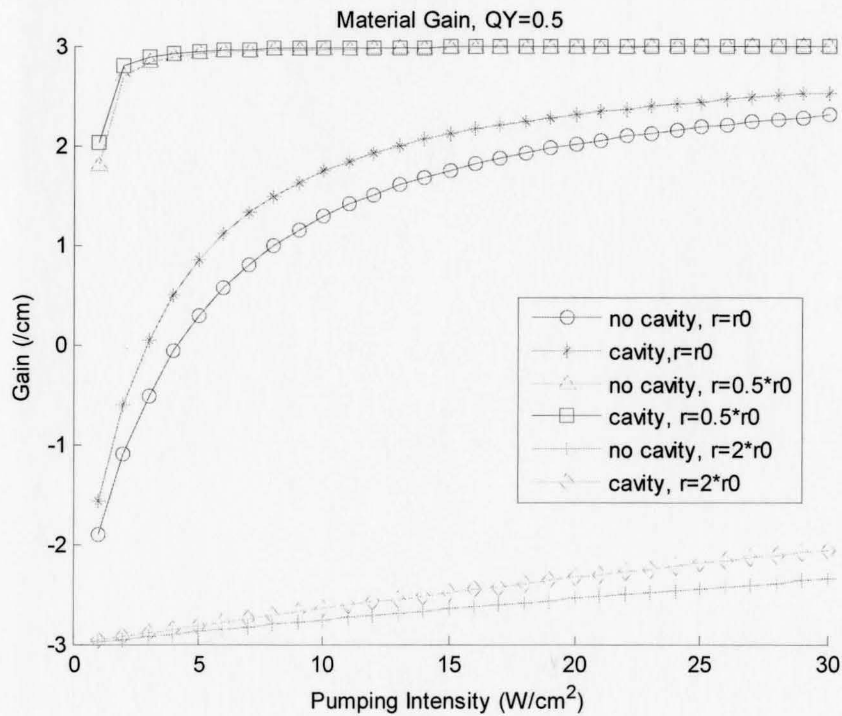

Figure 3-6 Material gain for metal cavity with QY=0.5.

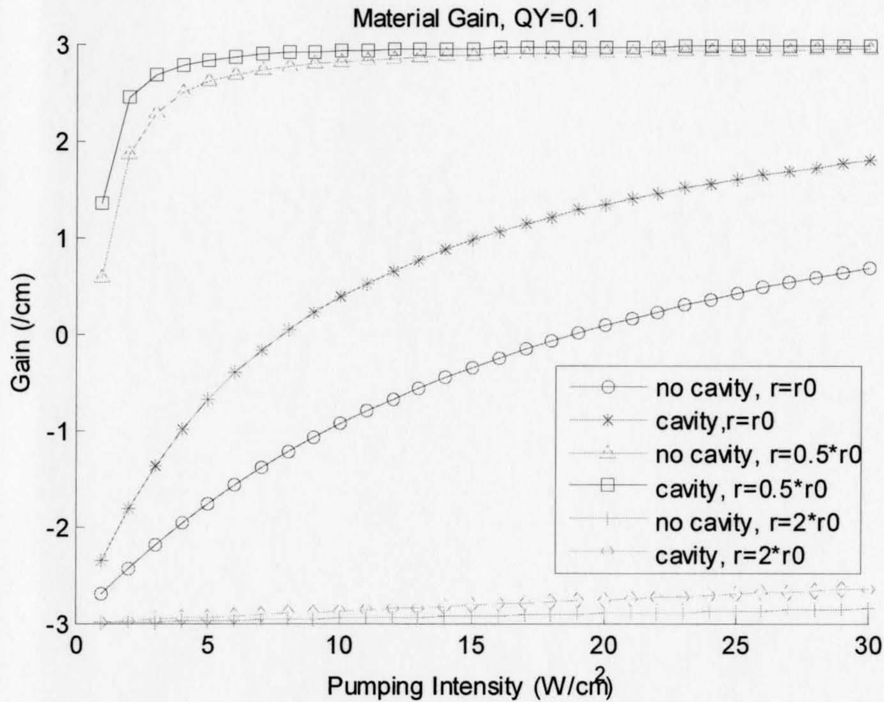

Figure 3-7 Material gain for metal cavity with QY=0.1.

To drastically increase the rate of Forster energy transfer, we have to apply a strong confined cavity, such as slot waveguide or micro-ring. It can not only increase the donor transition rate by quantum electrodynamic effect, but also increase the critical distance R_0 through the overlap integral with cavity effect. This enhancement will efficiently increase the acceptor emission, thus the material gain.

3.4 Green's Function Simulation for Multilayer

As we discussed in Chapter 2, Green's function is the solution of the wave equation for a point source (dipole). It is an old electrodynamic problem, but very tricky

to deal with [24][25]. We are going to discuss the Green's tensor $\overleftrightarrow{\mathbf{G}}(\mathbf{r},\mathbf{r}')$ in multilayer media [26].

The Green's tensor $\overleftrightarrow{\mathbf{G}}(\mathbf{r},\mathbf{r}')$ represents the electric field radiated at position $\mathbf{r}$ by three orthogonal dipoles located at $\mathbf{r}'$. For an arbitrary scattering system with dielectric permittivity $\varepsilon(\mathbf{r})$ and magnetic permeability $\mu(\mathbf{r})$, $\overleftrightarrow{\mathbf{G}}(\mathbf{r},\mathbf{r}')$ is the solution of the vector wave equation with a point source given by

$$\nabla\times\mu^{-1}(\mathbf{r})\nabla\times\overleftrightarrow{\mathbf{G}}(\mathbf{r},\mathbf{r}')-k_0^2\varepsilon(\mathbf{r})\nabla\times\overleftrightarrow{\mathbf{G}}(\mathbf{r},\mathbf{r}')=\mu^{-1}(\mathbf{r})\mathbf{1}\delta(\mathbf{r},\mathbf{r}') \tag{3.13}$$

where $k_0=\omega\sqrt{\varepsilon_0\mu_0}$ is the free space wave number. For a homogeneous medium with $\varepsilon_B=\varepsilon_0\varepsilon_r$, $\mu_B=\mu_0\mu_r$, the solution is well known:

$$\begin{aligned}\overleftrightarrow{\mathbf{G}}_H(\mathbf{r},\mathbf{r}')&=\left(1+\frac{\nabla\nabla}{k_B^2}\right)\frac{\exp(ik_BR)}{4\pi R}\\&=\left(\mathbf{1}+\frac{ik_BR-1}{k_B^2R^2}\mathbf{1}+\frac{3-3ik_BR-k_B^2R^2}{k_B^2R^4}\mathbf{RR}\right)\frac{\exp(ik_BR)}{4\pi R}\end{aligned} \tag{3.14}$$

where $R=|\mathbf{R}|=|\mathbf{r}-\mathbf{r}'|$, $k_B=\omega\sqrt{\varepsilon_B\mu_B}$ is the background wave number.

The multilayer medium is shown in Figure 3-8. We assume the layers are perpendicular to z-axis, and each layer extends to infinity in x and y directions, with ε_l and μ_l.

A convenient way to deal with multilayer structure is to use the Fourier transformation, and integrate in the k-domain. Eq. (3.14) is therefore

$$\overleftrightarrow{\mathbf{G}}_H(\mathbf{r},\mathbf{r}')=\frac{1}{8\pi^3k_B^2}\iiint\left(\frac{\mathbf{1}k_B^2-\mathbf{kk}}{k^2-k_B^2}\right)\exp(i\mathbf{k}\cdot\mathbf{R})d\mathbf{k} \tag{3.15}$$

Perform the integration over k_z using calculus of residues, and we can obtain

$$\overleftrightarrow{\mathbf{G}}_H(\mathbf{r},\mathbf{r}') = \frac{i}{8\pi^2 k_B^2}\iint\left(\frac{\mathbf{1}k_B^2 - \mathbf{k}_B\mathbf{k}_B}{k_{Bz}}\right)\exp(i\mathbf{k}_B\cdot\mathbf{R})\,dk_x dk_y - \frac{\hat{\mathbf{z}}\hat{\mathbf{z}}}{k_B^2}\delta(\mathbf{R}) \tag{3.16}$$

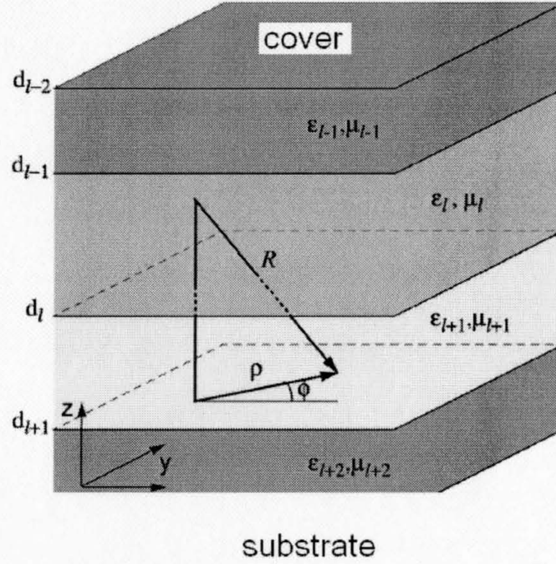

Figure 3-8 Multilayer system consisting of N layers. [26]

where $k_{Bz} = \left(k_B^2 - k_x^2 - k_y^2\right)^{1/2}$ is the z component of the wave vector,

$$\mathbf{k}_B(k_{Bz}) = \begin{cases} k_x\hat{\mathbf{x}} + k_y\hat{\mathbf{y}} + k_{Bz}\hat{\mathbf{z}}, & z > z' \\ k_x\hat{\mathbf{x}} + k_y\hat{\mathbf{y}} - k_{Bz}\hat{\mathbf{z}}, & z < z' \end{cases} \tag{3.17}$$

If we add additional layers, we have to account in the upward and downward propagating waves. Based on the propagation direction $\mathbf{k}$, we can introduce a new orthonormal coordinate system for $z > z'$

$$\begin{aligned}
\hat{\mathbf{k}}(k_{Bz}) &= \frac{\mathbf{k}_B(k_{Bz})}{k_B} \\
\hat{\mathbf{l}}(k_{Bz}) &= \frac{\hat{\mathbf{k}}(k_{Bz})\times\hat{\mathbf{z}}}{\left|\hat{\mathbf{k}}(k_{Bz})\times\hat{\mathbf{z}}\right|} = \hat{\mathbf{x}}\frac{k_y}{\sqrt{k_x^2+k_y^2}} - \hat{\mathbf{y}}\frac{k_x}{\sqrt{k_x^2+k_y^2}} \\
\hat{\mathbf{m}}(k_{Bz}) &= \hat{\mathbf{k}}(k_{Bz})\times\hat{\mathbf{l}}(k_{Bz}) = \hat{\mathbf{x}}\frac{k_x k_{Bz}}{k_B\sqrt{k_x^2+k_y^2}} - \hat{\mathbf{y}}\frac{k_y k_{Bz}}{k_B\sqrt{k_x^2+k_y^2}} - \hat{\mathbf{z}}\frac{\sqrt{k_x^2+k_y^2}}{k_B}
\end{aligned} \tag{3.18}$$

When $z < z'$, we form another orthonormal system $\hat{\mathbf{k}}(-k_{Bz})$, $\hat{\mathbf{l}}(-k_{Bz})$, $\hat{\mathbf{m}}(-k_{Bz})$. For a given k_B, the electric field parallel to $\hat{\mathbf{l}}$ corresponds to s polarization, i.e. TE wave; the electric field parallel to $\hat{\mathbf{m}}$ corresponds to p polarization, i.e. TM wave. Eq. (3.16) can be written as

$$\overleftrightarrow{\mathbf{G}}_H(\mathbf{r},\mathbf{r}') = \frac{i}{8\pi^2}\iint\left(\frac{\hat{\mathbf{l}}\hat{\mathbf{l}}+\hat{\mathbf{m}}\hat{\mathbf{m}}}{k_{Bz}}\right)\exp(i\mathbf{k}_B\cdot\mathbf{R})\,dk_x dk_y - \frac{\hat{\mathbf{z}}\hat{\mathbf{z}}}{k_B^2}\delta(\mathbf{R}) \tag{3.19}$$

For l-th layer, each component of Green's tensor can be expressed in terms of s- and p-polarized upgoing and downgoing plane waves, with amplitude coefficients $A^s_{l,\alpha\beta}, B^s_{l,\alpha\beta}, A^p_{l,\alpha\beta}, B^p_{l,\alpha\beta}$:

$$\begin{aligned}
G_{\alpha\beta}(\mathbf{r},\mathbf{r}') = &-\frac{\hat{\mathbf{z}}\hat{\mathbf{z}}}{k_B^2}\delta(\mathbf{R}) + \frac{i}{8\pi^2}\iint dk_x dk_y \exp\left\{i\left[k_x(x-x')+k_y(y-y')\right]\right\}\frac{1}{k_{lz}} \\
&\left\{\left[\hat{l}_\alpha(\pm k_{lz})A^s_{l,\alpha\beta}\exp(ik_{lz}z)+\hat{l}_\alpha(\mp k_{lz})B^s_{l,\alpha\beta}\exp(-ik_{lz}z)\right]\hat{l}_\beta(k_{lz})\right. \\
&\left.+\left[\hat{m}_\alpha(\pm k_{lz})A^p_{l,\alpha\beta}\exp(ik_{lz}z)+\hat{m}_\alpha(\mp k_{lz})B^p_{l,\alpha\beta}\exp(-ik_{lz}z)\right]\hat{m}_\beta(k_{lz})\right\}
\end{aligned} \tag{3.20}$$

where the upper sign is for $z > z'$, and the lower sign for $z < z'$. The amplitude coefficients are derived from boundary conditions, and related to the source. The boundary conditions are the continuity equations at each interface from Maxwell's equations:

$$\hat{\mathbf{z}} \times \left(\overleftrightarrow{\mathbf{G}}^{+} - \overleftrightarrow{\mathbf{G}}^{-} \right) = 0 \tag{3.21}$$

$$\hat{\mathbf{z}} \cdot \left(\varepsilon^{+} \overleftrightarrow{\mathbf{G}}^{+} - \varepsilon^{-} \overleftrightarrow{\mathbf{G}}^{-} \right) = 0 \tag{3.22}$$

$$\hat{\mathbf{z}} \times \nabla \times \left(\frac{\overleftrightarrow{\mathbf{G}}^{+}}{\mu^{+}} - \frac{\overleftrightarrow{\mathbf{G}}^{-}}{\mu^{-}} \right) = 0 \tag{3.23}$$

$$\hat{\mathbf{z}} \cdot \nabla \times \left(\overleftrightarrow{\mathbf{G}}^{+} - \overleftrightarrow{\mathbf{G}}^{-} \right) = 0 \tag{3.24}$$

where the superscript $+$ denotes the quantities just above the interface, and $-$ the quantities just below the interface. When $z > z'$, no field is reflected from $z = \infty$, thus $B_{1,\alpha\beta} = 0$. We can iteratively calculate the amplitude ratio B_l / A_l till the source layer l'. When $z < z'$, no field is reflected from $z = -\infty$, thus $A_{N,\alpha\beta} = 0$. We can iteratively get A_l / B_l for layers $N-1, N-2, ..., l'$.

In the source layer, we have to consider the source term $\hat{l}_\alpha(k_{l'z})\hat{l}_\beta(k_{l'z})\exp(ik_{l'z}|z-z'|)$ for s-polarization, or $\hat{m}_\alpha(k_{l'z})\hat{m}_\beta(k_{l'z})\exp(ik_{l'z}|z-z'|)$ for p-polarization. This determines the amplitude coefficients $A^s_{l',\alpha\beta}, B^s_{l',\alpha\beta}, A^p_{l',\alpha\beta}, B^p_{l',\alpha\beta}$ in the source layer. Based on these source layer coefficients, we can use iteration to get the amplitude coefficients in every layer. Detailed formulations are referred to [26].

If we introduce the cylindrical coordinate system, Eq. (3.20) can be simplified further. The transverse coordinate $\boldsymbol{\rho}$ is given by

$$\boldsymbol{\rho} = (\rho\cos\phi, \rho\sin\phi) = (x - x', y - y') \tag{3.25}$$

and the transverse wave vector $\mathbf{k}_\rho$ is

$$\mathbf{k}_\rho = \left(k_\rho \cos k_\phi, k_\rho \sin k_\phi\right) = \left(k_x, k_y\right) \tag{3.26}$$

The integration over k_ϕ results in the Bessel functions

$$J_n\left(k_\rho \rho\right) = \frac{i^{-n}}{2\pi} \int_0^{2\pi} dk_\phi \exp\left(ik_\rho \rho \cos k_\phi\right) \cos\left(nk_\phi\right) \tag{3.27}$$

Therefore, we only need to do numerical integration over the radial wave vector k_ρ:

$$\overleftrightarrow{\mathbf{G}}(\mathbf{r},\mathbf{r}') = -\frac{\hat{\mathbf{z}}\hat{\mathbf{z}}}{k_B^2}\delta(\mathbf{R}) + \frac{i}{4\pi}\int_0^\infty dk_\rho \left[\mathbf{f}^s\left(k_\rho;\mathbf{r},\mathbf{r}'\right) + \mathbf{f}^p\left(k_\rho;\mathbf{r},\mathbf{r}'\right)\right] \tag{3.28}$$

where the integrand tensors $\mathbf{f}^s$ and $\mathbf{f}^p$ can be expressed in terms of $A^s_{l,\alpha\beta}, B^s_{l,\alpha\beta}, A^p_{l,\alpha\beta}, B^p_{l,\alpha\beta}$.

The semi-infinite integral in Eq. (3.28) is the famous Sommerfeld integral. The integrand is typically in the form of

$$f\left(k_\rho;\mathbf{r},\mathbf{r}'\right) = g\left(k_\rho;\mathbf{r},\mathbf{r}'\right) J_n\left(k_\rho \rho\right)\left[A\left(k_\rho, z'\right)\exp\left(ik_{lz}z\right) + B\left(k_\rho, z'\right)\exp\left(-ik_{lz}z\right)\right] \tag{3.29}$$

This kind of integral has to be numerically calculated. However, two difficulties have to be solved.

One difficulty is the singularities of $f\left(k_\rho;\mathbf{r},\mathbf{r}'\right)$. Two types of singularities exist: branch point singularities and pole singularities. Branch point singularities are related to $k_{lz} = \left(k_l^2 - k_\rho^2\right)^{1/2}$ in the integrand. The square root is double-valued, and the branch points appear at $k_\rho = \pm k_1, \pm k_N$. We can use the radiation condition, i.e. force integrands to vanish when $z \to \pm\infty$. Thus we force the imaginary part of k_{lz} to be positive.

The pole singularities are related to guided modes in multilayer waveguide theory. For lossless media, the propagation vectors of the guided modes have to be smaller than the larges wavenumber of layers, i.e. $k_l^{\max} = \max_l \mathrm{Re}(k_l)$. For lossy media, $\mathrm{Im}(\varepsilon) > 0$, the branch and pole singularities are shifted to the first quadrant of the complex k_ρ plane.

To avoid pole singularities, one category of methods is to draw a semicircle around each singularity, and use the analytical value of the pole. This requires the exact determination of the pole locations. Here we follow the elliptical path integral approach, shown in Figure 3-9. We draw an elliptical path in the fourth quadrant, starting at $k_\rho = 0$ and with the major semiaxis k_ρ^{maj} and the minor semiaxis $k_\rho^{\min}$. The elliptic should enclose all of the poles, thus we choose $2k_\rho^{\mathrm{maj}} = k_l^{\max} + ck_0$, where k_0 is the free space wave number as a safety margin, and $0 < c \le 1$ is an adjusting coefficient. For $k_\rho^{\min}$, it can be chosen empirically to be $k_\rho^{\min} = 10^{-3} k_\rho^{\mathrm{maj}}$ so that the path is far away from poles on the real axis, while not extending too much in negative imaginary k_ρ direction.

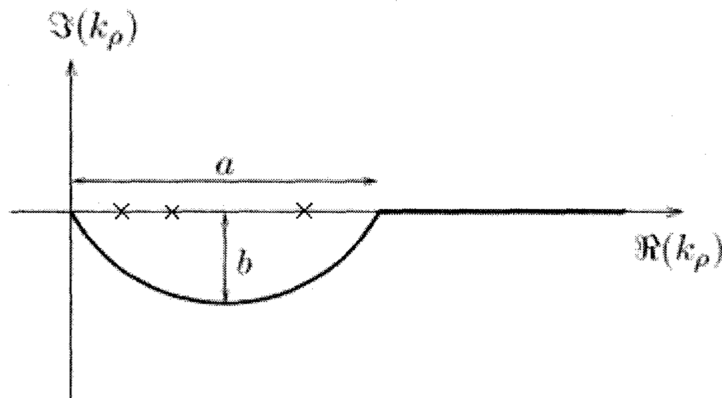

Figure 3-9 Contour deformation in complex k_ρ plane.

For the Sommerfeld integral tail of k_ρ beyond poles to infinity, the Bessel functions have big oscillations. One approach is the extrapolation method [27]. Here, we adopt another method. First, transform Bessel functions to Hankel functions

$$J_n\left(k_\rho \rho\right)=\frac{1}{2}\left\{H_n^{(1)}\left(k_\rho \rho\right)+\left[H_n^{(1)}\left(\left(k_\rho \rho\right)^*\right)\right]^*\right\} \tag{3.30}$$

where $H_n^{(1)}\left(k_\rho \rho\right)$ is Hankel function of the first type, with the asymptotic behavior

$$\lim_{|k_\rho \rho|\to\infty} H_n^{(1)}\left(k_\rho \rho\right)=\sqrt{\frac{2}{\pi k_\rho \rho}}\exp\left[ik_\rho \rho-\frac{1}{2}i\pi\left(n+\frac{1}{2}\right)\right] \tag{3.31}$$

The Hankel functions exponentially decay, providing the excellent convergence for integration. Figure 3-10 is the comparison of Bessel function along real axis and Hankel function along imaginary axis. Thus we can deflect the integration path from real axis to a path parallel to the imaginary axis. For the first term in Eq. (3.30), we assign the positive imaginary path, and for the second term, we assign the negative imaginary path. We use the Gauss-Kronrod quadrature to calculate the numerical integration for Bessel and Hankel functions.

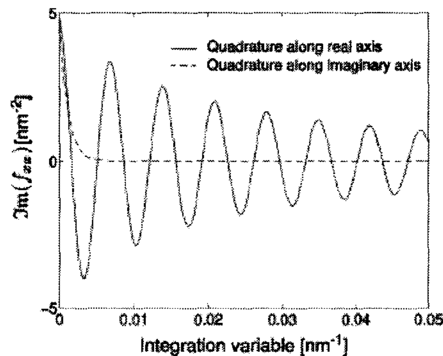

Figure 3-10 Comparison of Bessel function along real axis and Hankel function along imaginary axis.

To test the accuracy of this method, we compare the Green's tensor for homogeneous medium using integral approach described above with the analytical solution in Eq. (3.14). The result is shown in Figure 3-11. The two solutions match well.

Now we test the 4-layer medium with $\varepsilon_1 = 1$, $\varepsilon_2 = 2$, $\varepsilon_3 = 10$, and $\varepsilon_4 = 1$. The emission wavelength is $\lambda = 633$ nm. Each layer has a thickness of 500 nm. We put the source at $\mathbf{r}' = (0, 0, 750\text{ nm})$, and observe the *xx* component of Green's tensor for *s*-polarization as a function of z at field points $\mathbf{r} = (\rho, \phi, z) = (\lambda, \pi/4, z)$. Figure 3-12 represents the *x* component of the electric field radiated by an *x*-oriented dipole. In the inner layers, the dipole excites standing waves. For *s*-polarization, the electric field is continuous across all the interfaces.

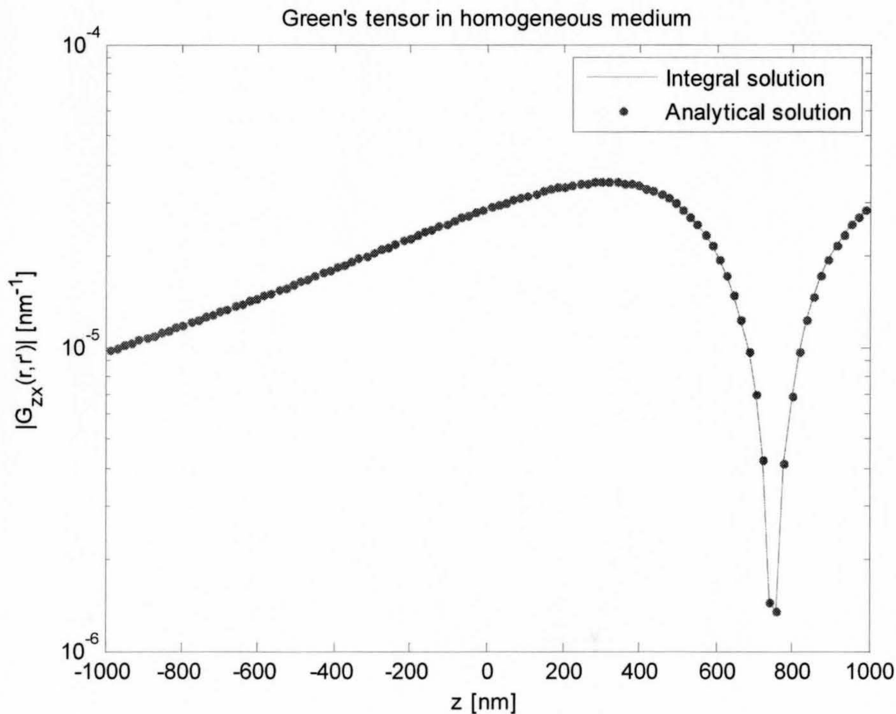

Figure 3-11 Green's tensor in inhomogeneous medium.

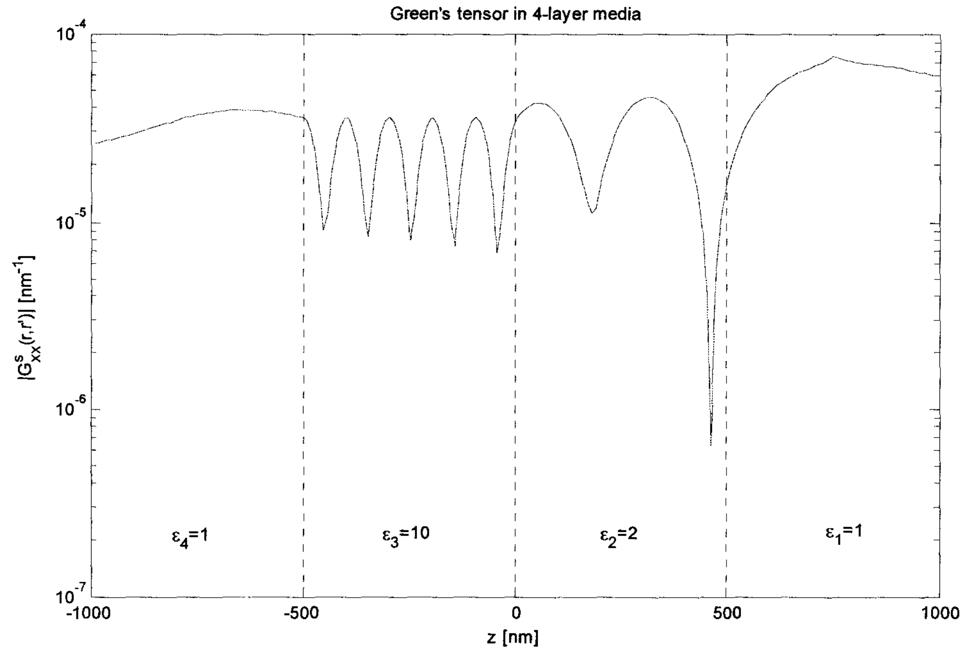

Figure 3-12 Green's tensor in 4-layer media.

3.5 Summary and Future work

In this chapter we discuss the material gain modification for a metal cavity and a general multilayer system. We can see that even for 1D cavity where light is loosely confined, the requirement of optical pumping is greatly reduced.

There are still some critical numerical problems unsolved for Green's tensor calculation in multilayer systems. I shall continue on this subject and obtain a stable solver compatible to other structures, e.g. slot waveguide, or Bragg waveguide.

After the exact calculation of Green's tensor, we shall apply the theory in Chapter 2 to get the energy transfer rate, and further obtain the material gain.

Chapter 4.

Silicon Nanocrystal in Electric Field

4.1 Introduction

The electrically-pumped silicon laser is what we desire. Up to now, the most promising approach is based on metal-oxide-semiconductor (MOS) structures with Er implanted in the thin gate oxide formed by Si-nc embedded in SiO_2. The hot electron transport through the gate oxide is attributed to Fowler-Nordheim tunneling [28][29].

Here we will not investigate tunneling effect for the time being. Instead, we will study the Si-nc in electric field using a quantum dot model. We will first look at the variational method and the band structure of silicon. Based on that, we will calculate the silicon transition energy and rate in electric field. We study both the "quasi"-direct transition and the phonon-assisted transition.

4.2 Variational Method

In quantum mechanics [30], the time-independent Schrodinger equation is

$$H\psi = E\psi \tag{4.1}$$

where H is the Hamiltonian, E is the eigenvalue, and ψ is the wave function. If we want to calculate the ground state energy E_{gs} when Eq. (4.1) is hard to solve, we can get

an upper bound for E_{gs} using the variational principle. Any normalized function ψ satisfies

$$E_{gs} \leq \langle \psi | H | \psi \rangle \equiv \langle H \rangle \tag{4.2}$$

Thus we can pick a trial function with some parameters, work out the expectation value of the Hamiltonian, and minimize it. In this way, we obtain the wavefunction and the corresponding energy. If the trial function is well chosen, the results can be very close to the actual ground state function and energy. We are going to use this method to deal with the quantum-confined Stark effect.

4.3 Band Structure of Silicon

Silicon is an indirect bandgap semiconductor material [31]. The band structure of Si is shown in Figure 4-1. The maximum of valance band is at Γ-point; the minimum of conduction band is along the ΓX (1,0,0) direction, located at $k_0 = 0.85(2\pi / a)$, where $a = 5.43$ Å is the lattice constant of Si.

Owing to the cubic symmetry of the band structure of Si, there are 6 minima of conduction band on the star of ΓX lines altogether (shown in Figure 4-2). The vicinities of the minima is named valleys, and Si has 6 valleys, centered at the points

$(k_0, 0,0)$, $(0, k_0, 0)$, $(0,0,k_0)$, $(-k_0, 0,0)$, $(0,-k_0, 0)$, $(0,0,-k_0)$

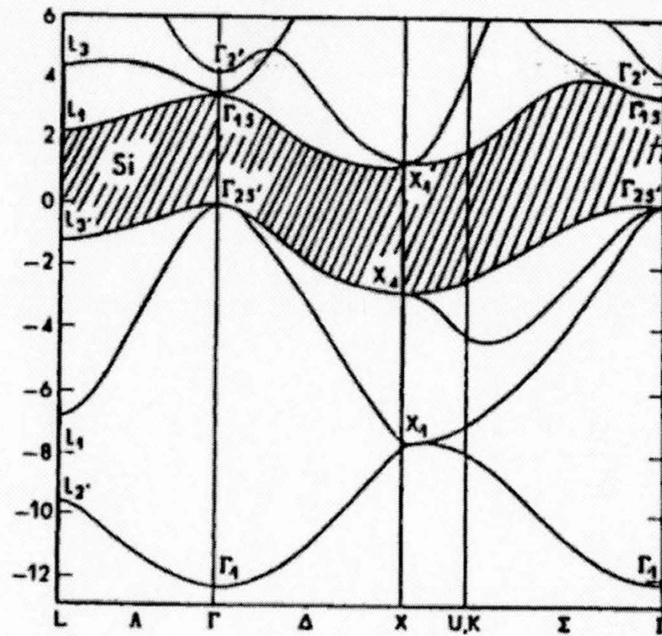

Figure 4-1 Band structure of Si. The energy unit is eV. [31]

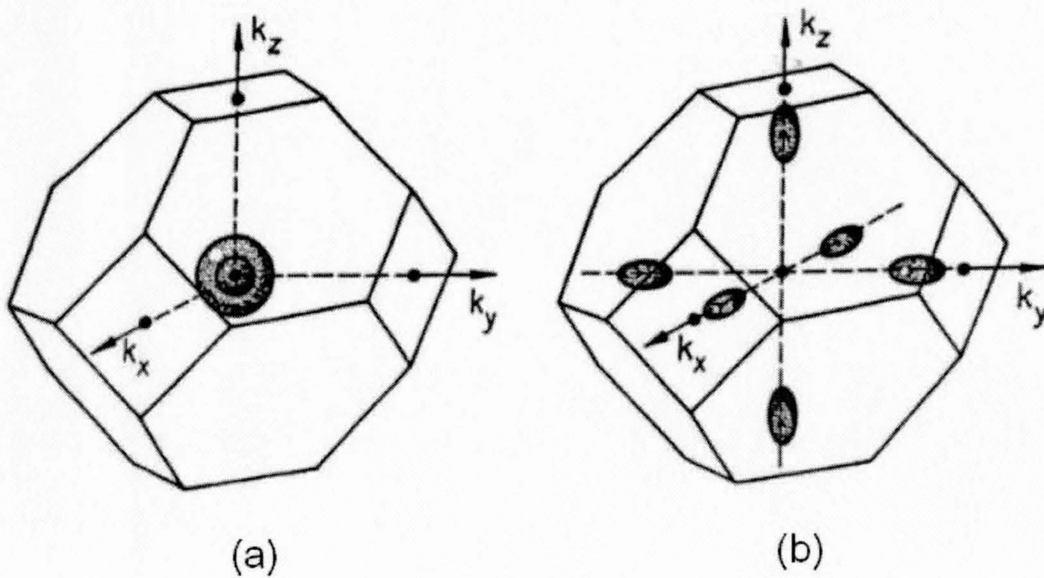

Figure 4-2 Iso-energy surfaces of the holes (a) and electrons (b). [31]

Without loss of generality, we select the valley centered at (k_0,0,0). If we put the origin at Γ point, the dispersion relation $E_c(\mathbf{k})$ of this band is given by

$$E_c(\mathbf{k}) = E_g + \frac{\hbar^2}{2m_{el}}(k_x - k_0)^2 + \frac{\hbar^2}{2m_{et}}(k_y^2 + k_z^2) \tag{4.3}$$

where $E_g = 1.12eV$ is the fundamental energy gap of Si, $m_{el} = 0.92m_0$ is the effective longitudinal electron mass, and $m_{et} = 0.19m_0$ is the effective transverse electron mass. m_0 is the mass of electron.

For hole in valence band, the dispersion relation is

$$E_v(\mathbf{k}) = -\frac{\hbar^2}{2m_h}(k_x^2 + k_y^2 + k_z^2) \tag{4.4}$$

where $m_h = 0.54m_0$ is the effective mass of the (heavy) hole.

We adopt the nonparabolic approximation, and the kinetic energy

$$E_{kin0} = \frac{\hbar^2 k^2}{2m} = E_{kin}(1 + \alpha E_{kin}) \tag{4.5}$$

We can obtain the better expectation value of kinetic energy

$$\langle E_{kin} \rangle = \frac{-1 + \sqrt{1 + 4\alpha \langle E_{kin0} \rangle}}{2\alpha} \tag{4.6}$$

For electron, $\alpha_e = 0.2eV^{-1}$; for hole, $\alpha_h = 0.5eV^{-1}$.

4.4 Wavefunction of Si-nc in Electric Field

Suppose there is one Si-nc embedded in an amorphous SiO_2 matrix, and the system is placed in a strong electric field [32]. The barriers between bulk Si and SiO_2 are

around 3.2 eV and 4.5 eV for electrons and holes, respectively. The breakdown field of SiO_2 can be very large (around 10 MV/cm), therefore it is possible to apply electric field up to 6 to 8 MV/cm.

For simplicity, we treat Si-nc as a cubic quantum dot with infinite barrier heights. Suppose the cubic oriented along the (1,0,0) direction, and we apply electric field F also along (1,0,0) direction. Imagine if there is no electric field, the wave functions of electron and hole will center at the center of the cubic. After applying electric field, hole is pushed against the direction of the field, while electron is pushed along the field. In the following text, the subscript e is for electron in conduction band, and h for hole in valence band.

Based on the well-known wavefunction of 1D infinite quantum well, we can write down the envelope wave functions in spatial domain

$$\psi_e(\mathbf{r}) = \frac{2}{L} b_e \sin\left(\frac{\pi x}{L}\right) \sin\left(\frac{\pi y}{L}\right) \sin\left(\frac{\pi z}{L}\right) \exp\left(-\frac{a_e x}{2}\right) \tag{4.7}$$

$$\psi_h(\mathbf{r}) = \frac{2}{L} b_h \sin\left(\frac{\pi (L-x)}{L}\right) \sin\left(\frac{\pi y}{L}\right) \sin\left(\frac{\pi z}{L}\right) \exp\left(-\frac{a_h (L-x)}{2}\right) \tag{4.8}$$

where L is the cubic size, $a_{e,h}$ is the variational parameter, and $b_{e,h}$ is the normalization factor

$$\int_0^L \int_0^L \int_0^L \psi_{e,h}^2(\mathbf{r})\, dxdydz = 1 \tag{4.9}$$

$$b_{e,h} = \sqrt{\frac{a_{e,h}\left(a_{e,h}^2 L^2 + 4\pi^2\right)}{2\pi^2\left(1 - \exp\left(-a_{e,h} L\right)\right)}} \tag{4.10}$$

The degeneracy of the 6 valleys will be lifted by electric field to 2 groups. One group is the two valleys with ellipsoid major axes along the electric field, called lower

valleys. The other group is the left four valleys, called upper valleys. Since the minimum of Si conduction band is shifted by k_0 in momentum space, it is more convenient to conduct our calculations in momentum space. Using Fourier transform

$$\psi(\mathbf{k}) = \frac{1}{(2\pi)^{3/2}} \int_0^L \int_0^L \int_0^L \psi(\mathbf{r}) \exp(-ik_x x - ik_y y - ik_z z)\, dxdydz \tag{4.11}$$

For hole, we obtain

$$\psi_h(k_x, k_y, k_z) = L^2 (2\pi)^{\frac{3}{2}} b_h \frac{\exp(-ik_x L) + \exp\left(-\frac{1}{2} a_h L\right)}{4\pi^2 + L^2 (a_h - 2ik_x)^2} \bullet \frac{1 + \exp(-ik_y L)}{\pi^2 - k_y^2 L^2} \frac{1 + \exp(-ik_z L)}{\pi^2 - k_z^2 L^2} \tag{4.12}$$

For electron,

$$\psi_k(k_x, k_y, k_z) = L^2 (2\pi)^{\frac{3}{2}} b_e \frac{1 + \exp\left(-ik_x L - \frac{1}{2} a_e L\right)}{4\pi^2 + L^2 (a_e + 2ik_x)^2} \bullet \frac{1 + \exp(-ik_y L)}{\pi^2 - k_y^2 L^2} \frac{1 + \exp(-ik_z L)}{\pi^2 - k_z^2 L^2} \tag{4.13}$$

Noticing the k_0 shift, we get for lower valleys,

$$\psi_e(k_x, k_y, k_z) = \psi_k(k_x - k_0, k_y, k_z) \tag{4.14}$$

For upper valleys, without loss of generality,

$$\psi_e(k_x, k_y, k_z) = \psi_k(k_x, k_y - k_0, k_z) \tag{4.15}$$

For electric field in the MV/cm range, the energy interval between lower and upper valleys is much larger than $k_B T$, where k_B is the Boltzmann constant, and T is the

temperature. Thus for electron-hole pairs, the electron has a large probability to occupy the lower valley state, which we will focus on in the following discussions.

4.5 Transition Energy

Now we are ready to calculate the expectation values of the Hamiltonians for electron and hole.

$$E_e = \langle H \rangle_e = \langle E_{kin} \rangle_e + \langle V \rangle_e \tag{4.16}$$

For lower valleys, the kinetic energy is given by

$$\langle E_{kin0} \rangle_e = \int_{-\infty}^{\infty}\int_{-\infty}^{\infty}\int_{-\infty}^{\infty} \psi_e^*(\mathbf{k}) \left[\frac{\hbar^2}{2m_{el}}(k_x - k_0)^2 + \frac{\hbar^2}{2m_{et}}\left(k_y^2 + k_z^2\right) \right] \psi_e(\mathbf{k})\, dk_x dk_y dk_z \tag{4.17}$$

we can obtain

$$\langle E_{kin0} \rangle_e = \frac{\pi^2 b_e^2 \hbar^2}{4L^2 a_e}\left(1 - \exp(-2a_e L)\right) \left[\frac{1}{m_{el}} + \frac{8\pi^2}{m_{et}\left(4\pi^2 + L^2 a_e^2\right)} \right] \tag{4.18}$$

$$\langle E_{kin} \rangle_e = \frac{-1 + \sqrt{1 + 4\alpha_e \langle E_{kin0} \rangle_e}}{2\alpha_e} \tag{4.19}$$

The potential energy of electron in the electric field can be expressed as

$$\langle V \rangle_e = \langle |e| Fx \rangle_e \tag{4.20}$$

where e is the electron charge, F is the electric field, and x is the position operator. In momentum space, $x = i\dfrac{\partial}{\partial k_x}$, and the potential becomes

$$\langle |e|Fx \rangle_e = \int_{-\infty}^{\infty}\int_{-\infty}^{\infty}\int_{-\infty}^{\infty} \psi_e^*(\mathbf{k})|e|F\left(i\frac{\partial}{\partial k_x}\psi_e(\mathbf{k})\right)dk_x dk_y dk_z \tag{4.21}$$

After some evaluation, we get

$$\langle V \rangle_e = -\frac{2|e|Fb_e^2\pi^2}{a_e^2\left(4\pi^2 + L^2a_e^2\right)^2} \left\{\exp(-a_eL)\left(4\pi^2 + 4\pi^2a_eL + 3L^2a_e^2 + L^3a_e^3\right) - 4\pi^2 - 3L^2a_e^2\right\} \tag{4.22}$$

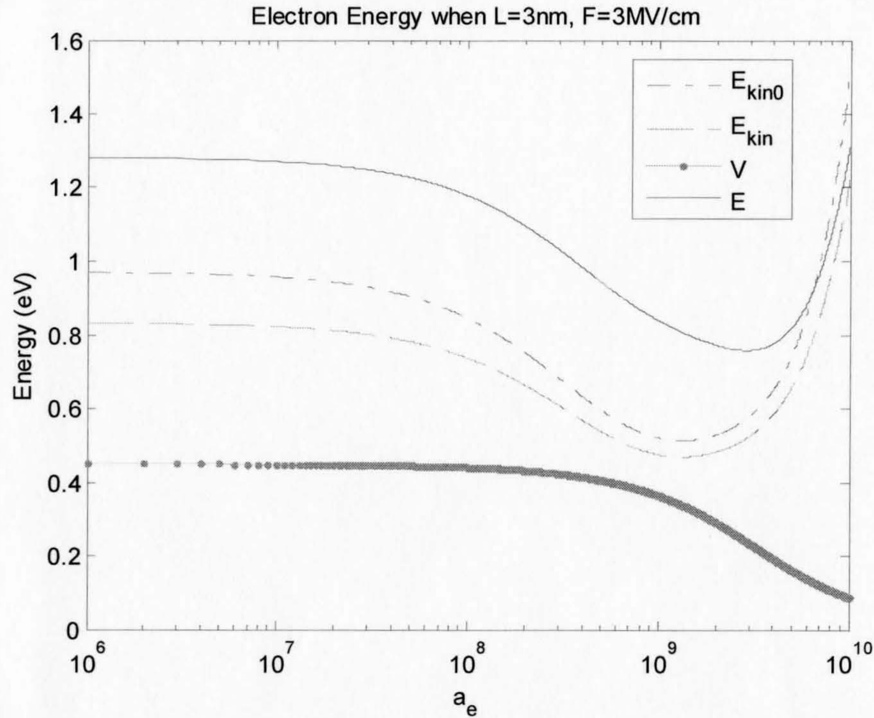

Figure 4-3 Electron energy as a function of variational parameter.

In Figure 4-3, the energies of electron as a function of a_e are shown, for the case $L = 3$ nm, $F = 3$ MV/cm . The black solid line is the total electron energy from Eq. (4.16).

For hole, we can follow the same procedure

$$E_h = \langle H \rangle_h = \langle E_{kin} \rangle_h + \langle V \rangle_h \tag{4.23}$$

$$\begin{aligned}\langle E_{kin0} \rangle_h &= \int_{-\infty}^{\infty}\int_{-\infty}^{\infty}\int_{-\infty}^{\infty} \psi_h^*(\mathbf{k})\left[\frac{\hbar^2}{2m_h}\left(k_x^2+k_y^2+k_z^2\right)\right]\psi_h(\mathbf{k})\,dk_x dk_y dk_z \\ &= \frac{1-\exp(-a_h L)}{4}\frac{\pi^2 b_h^2 \hbar^2}{L^2 a_h m_h}\frac{\left(a_h^2 L^2 + 12\pi^2\right)}{\left(a_h^2 L^2 + 4\pi^2\right)}\end{aligned} \tag{4.24}$$

$$\langle E_{kin} \rangle_h = \frac{-1+\sqrt{1+4\alpha_h \langle E_{kin0} \rangle_h}}{2\alpha_h} \tag{4.25}$$

$$\begin{aligned}\langle V \rangle_h &= \langle -|e|Fx \rangle_h = \int_{-\infty}^{\infty}\int_{-\infty}^{\infty}\int_{-\infty}^{\infty} -\psi_h^*(\mathbf{k})|e|F\left(i\frac{\partial}{\partial k_x}\psi_h(\mathbf{k})\right)dk_x dk_y dk_z \\ &= -\frac{2\pi^2 b_h^2 |e| F}{a_h^2\left(a_h^2 L^2 + 4\pi^2\right)^2}\left[4\pi^2\exp(-a_h L) + 3a_h^2 L^2 \exp(-a_h L) + a_h^3 L^3 - 3a_h^2 L^2 + 4\pi^2 a_h L - 4\pi^2\right]\end{aligned} \tag{4.26}$$

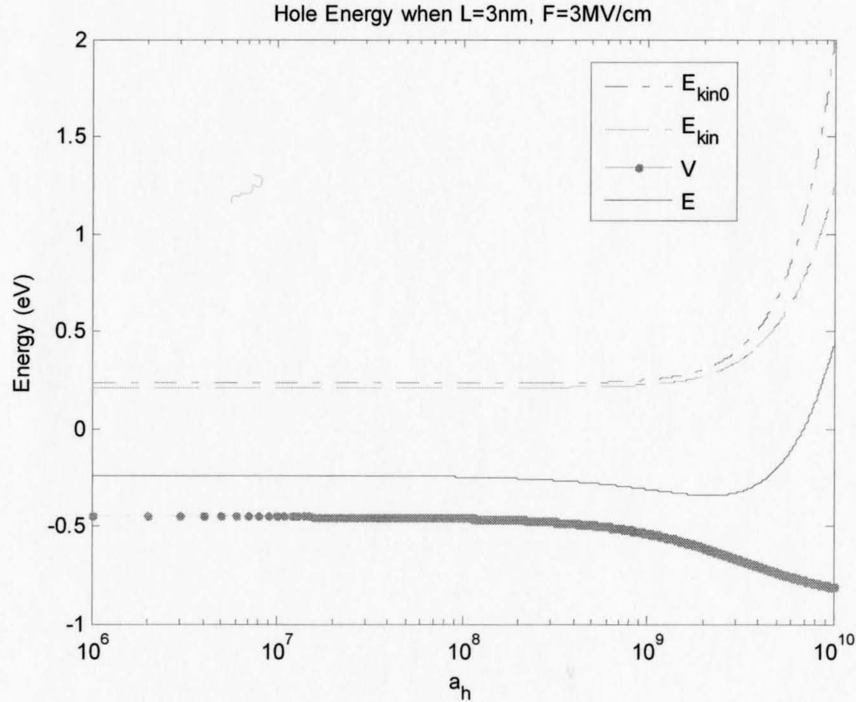

Figure 4-4 Hole energy as a function of variational parameter.

Figure 4-4 shows the energies of hole as a function of a_h, for the case $L = 3$ nm, $F = 3$ MV/cm. The black solid line is the total electron energy from Eq. (4.23).

We can find the parameters a_e and a_h corresponding to the minimum energies of electron and hole E_e, E_h, respectively. The minimum energies are approximately the ground state energies.

Now we study the variation of transition energies for Si-nc's with different cube sizes (from 1.5 nm to 4.5 nm) and in a range of electric field (from 0 to 7 MV/cm). The variational parameters are shown in Figure 4-5 for electrons and Figure 4-6 for holes.

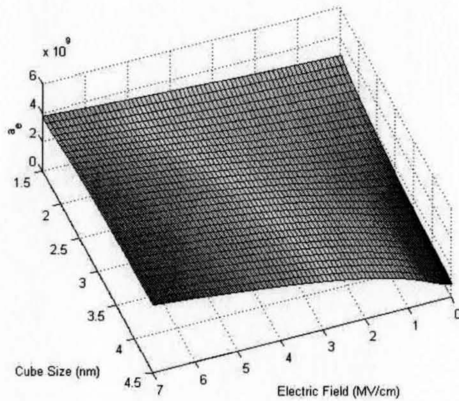

Figure 4-5 Variational parameters for electrons.

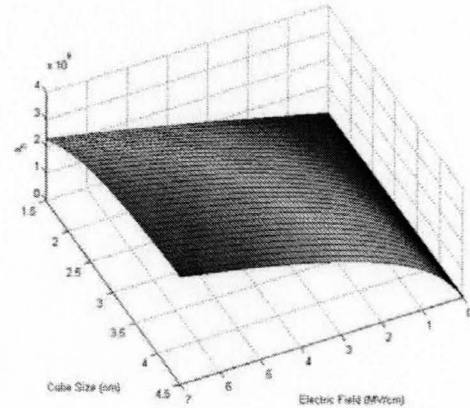

Figure 4-6 Variational parameters for holes.

In our approximation, we can neglect the high order electron and hole interactions, and write the transition energy as

$$E_0 = E_g + E_e + E_h \tag{4.27}$$

where $E_g = 1.12eV$ is the principle energy gap of silicon. We get the transition energies shown in Figure 4-7.

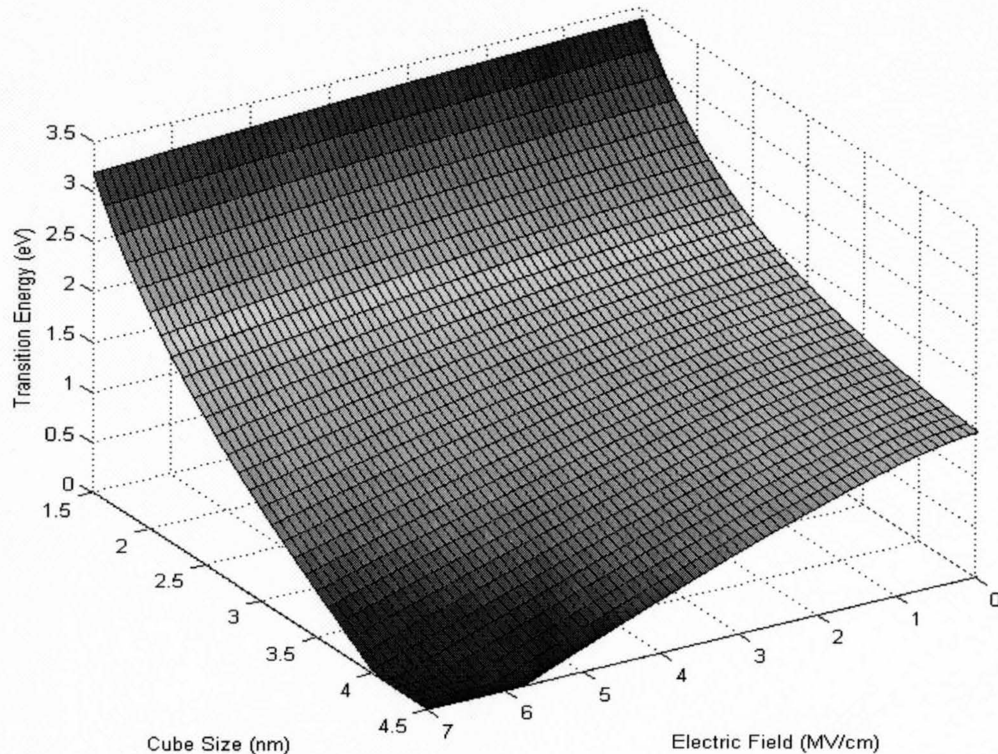

Figure 4-7 Transition energy for different size of Si-nc's in electric field.

We can see that when cube size is small, the transition energy becomes larger due to stronger confinement. If we apply stronger electric field, the transition energy will decrease correspondingly. For moderate electric fields, the energy shift is proportional to the square of electric field. This is the characteristic property for Stark effect, as predicted by the second order perturbation theory. When electric field becomes larger, or the cube size becomes greater, the energy gap disappears. We should use tunneling theory to model this range instead of the analysis here.

4.6 Transition Rate

Silicon has indirect band structure. When it becomes a quantum dot, the wave functions of electron and hole are confined in a small spatial area. Their wave functions spread in momentum space and overlap, making "quasi-direct" transition possible. The more they overlap, the easier the direct transition will be.

The direct transition rate is usually expressed by

$$\gamma_d = \frac{4\pi}{3} n \frac{q^2}{h^2 c^3 \varepsilon_0 m_0^2} E_0 \left| \langle f_{VB} \,|\, \mathbf{p} \,|\, i_{CB} \rangle \right|^2 \tag{4.28}$$

where E_0 is the transition energy, n is the refractive index of Si, h is Planck's constant, c is the light speed in free space, ε_0 is the permittivity in free space, and m_0 is the electron mass. $\langle f_{VB} \,|\, \mathbf{p} \,|\, i_{CB} \rangle$ is the momentum matrix between the final state of valence band and the initial state of conduction band. In the effective mass approximation, it can be given by

$$\langle f_{VB} \,|\, \mathbf{p} \,|\, i_{CB} \rangle = p_{cv} \int \psi_h(\mathbf{k}) \psi_e^*(\mathbf{k}) d\mathbf{k} \tag{4.29}$$

where $p_{cv} / 2m_0 = 4$ eV is the bulk value. For lower valleys, after some evaluations, we can obtain

$$\left| \langle f_{VB} \,|\, \mathbf{p} \,|\, i_{CB} \rangle \right|^2 = \frac{8\pi^4 b_e^2 b_h^2 p_{cv}^2 \exp(-\Omega_1 L)\left(\cosh(\Omega_2 L) - \cos(k_0 L)\right)}{16\pi^4 \left(\Omega_2^2 + k_0^2\right) + 8\pi^2 L^2 \left(\Omega_2^4 - k_0^4\right) + L^4 \left(\Omega_2^6 + k_0^6 + 3\Omega_2^4 k_0^2 + 3\Omega_2^2 k_0^4\right)} \tag{4.30}$$

where $\Omega_1 = (a_e + a_h)/2$, and $\Omega_2 = (a_e - a_h)/2$.

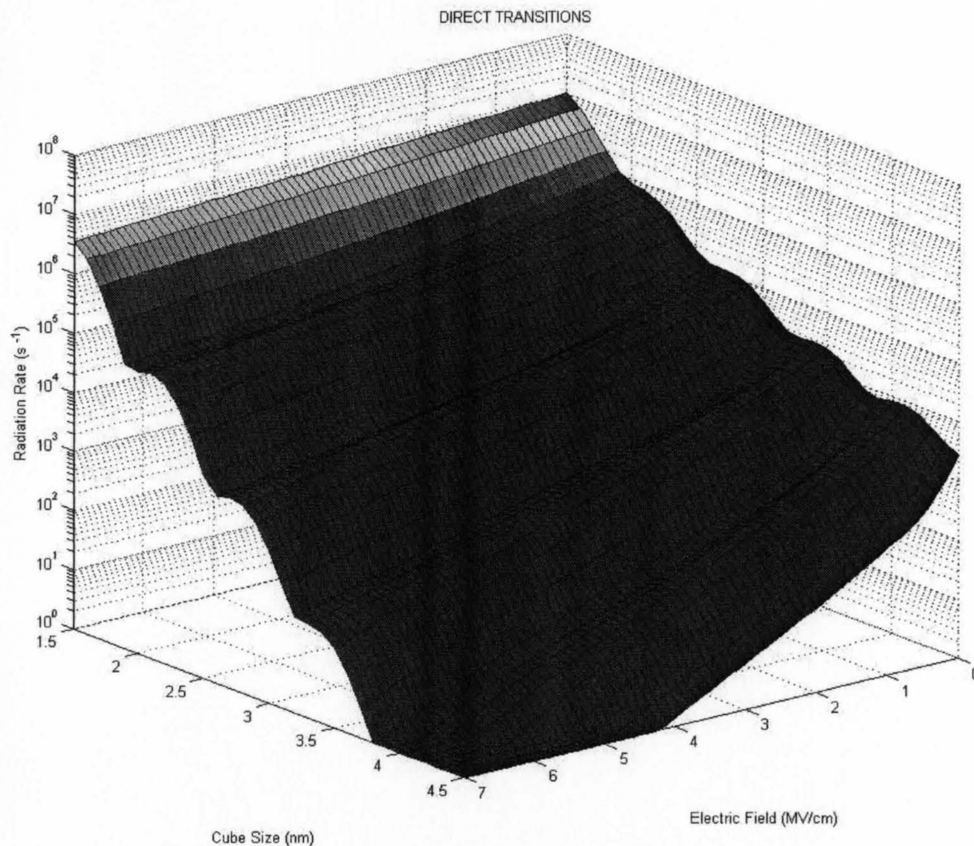

Figure 4-8 Radiation rate for direct transitions.

The calculation result of the radiation rate for direct transitions as a function of cube size and electric field is shown in Figure 4-8.When the cube size reduces, electron and hole are better confined, such that the direct transition is made easier, i.e., with higher probability. The electric field splits the wave functions, thus when the field is strong, the transition is slow. Our figure matches the theoretical expectation.

For indirect transition, i.e. phonon-assisted transition, we need to sum all possible momentum and polarization of phonon. For phonon with polarization λ, we can write [33]:

$$P_\lambda^2 = \left|\langle f_{VB} | \mathbf{p} | i_{CB} \rangle\right|_\lambda^2 = \frac{p_{cv}^2 R_\lambda^2}{d_{Si}} \int_0^L \int_0^L \int_0^L \left|\psi_e(\mathbf{r})\right|^2 \left|\psi_h(\mathbf{r})\right|^2 dxdydz \tag{4.31}$$

where d_{Si} is the atomic density of silicon, $d_{Si} = 5\times10^{22}$ atoms/cm^3 at $T = 300K$.

Substituting the spatial domain wave functions into Eq. (4.31), we obtain

$$P_\lambda^2 = \frac{27\pi^4 p_{cv}^2 R_\lambda^2 b_e^2 b_h^2 \exp(-\Omega_1 L)\sinh(\Omega_2 L)}{8 d_{Si} \Omega_2 L^2 \left(\Omega_2^2 L^2 + 4\pi^2\right)\left(\Omega_2^2 L^2 + \pi^2\right)} \tag{4.32}$$

Each phonon mode gives a distinct channel for absorption or emission of light. Here the transverse optic (TO) mode dominates, and longitudinal optic (LO) mode plays a smaller role. $R_{TO} = 0.08,\ \hbar\omega_{TO} = 57.5$ meV; $R_{LO} = 0.012,\ \hbar\omega_{TO} = 55.3$ meV.

At thermodynamic equilibrium, the occupation density of phonon modes n_λ is given by Bose-Einstein statistics

$$n_\lambda = \frac{1}{\exp\left(\hbar\omega_\lambda / k_B T\right) - 1} \tag{4.33}$$

For phonon absorption, the transition energy is given by

$$E_{0abs} = E_g + E_e + E_h - \hbar\omega_\lambda \tag{4.34}$$

while for phonon emission, the transition energy is

$$E_{0em} = E_g + E_e + E_h + \hbar\omega_\lambda \tag{4.35}$$

The indirect transition rate can be expressed by

$$\gamma_{ind} = \frac{4\pi}{3} n \frac{q^2}{h^2 c^3 \varepsilon_0 m_0^2} \sum_{\lambda=TO,LO} \left[E_{0abs} n_\lambda P_\lambda^2 + E_{0em} \left(n_\lambda + 1\right) P_\lambda^2 \right] \tag{4.36}$$

The calculated result of the radiation rate for phonon-assisted transitions as a function of cube size and electric field is shown in Figure 4-9. The trend is similar to

direct transitions. Comparing direct transitions with indirect ones, we find that when the cube size is smaller than 2.5 nm, the direct transitions play a greater role; otherwise, the phonon-assisted transitions play a greater role.

The electric field will hinder the radiation decay of Si-nc, but we have to further explore the tunneling mechanism before concluding the overall effect of electric field.

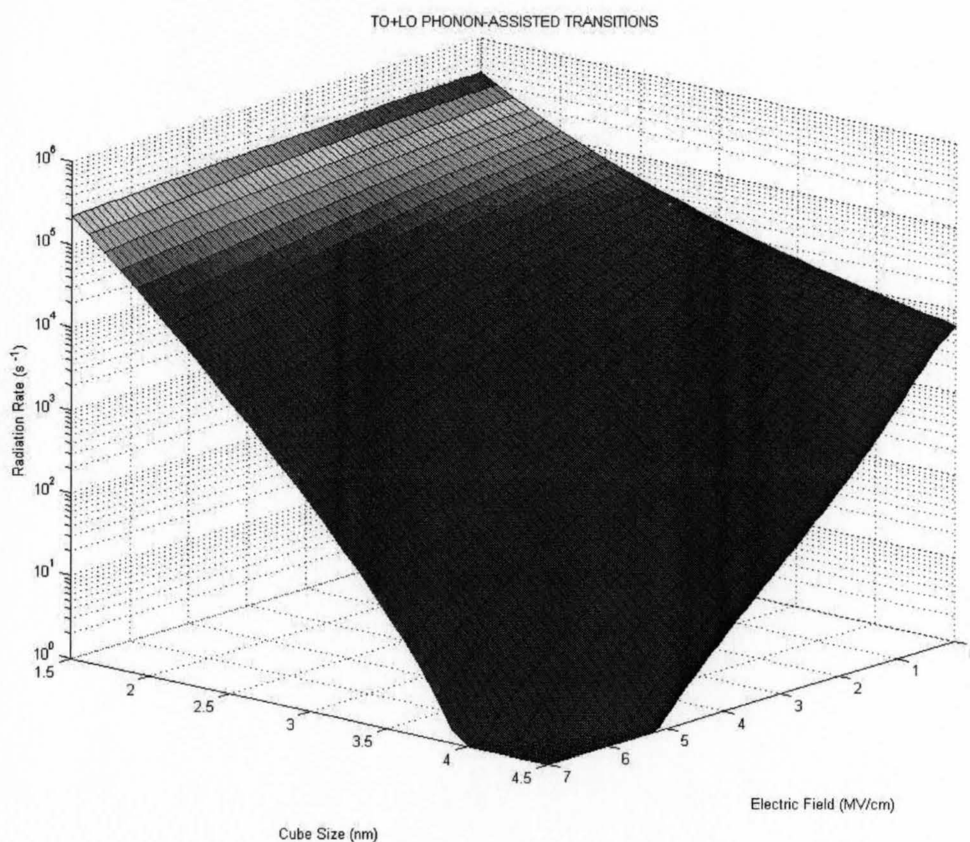

Figure 4-9 Radiation rate for phonon-assisted transitions.

Chapter 5.

Summary and Future work

The overall objectives of this study are the investigation of the effects of cavity and electric field on energy transfer between Si nanocrystals (Si-nc's) and Er ions, calculation of gain in such systems, and design of some optical devices based on the results of these studies.

In this thesis, we are actually dealing with one pair of Si-nc and Er ion. First, we give a brief introduction on silicon laser. In Chapter 2, we explore the dipole theories of spontaneous decay and energy transfer between two particles. It shows that for cavity effect on the energy transfer from Si-nc to Er ion, Green's function plays a crucial part. In Chapter 3, we use a simplified energy transfer model to describe a metal microcavity, come out with some primitive estimation. This has shown that microcavity could lead to significant improvements, reducing the requirements for Si-nc pumping. After that, we discuss the numerical accurate evaluation of Green's tensor in multilayer system. In Chapter 4, starting from the bandgap properties of silicon, we apply variational method to calculate how electric field affects the silicon transition energy and rate. We study the "quasi"-direct transition and the phonon-assisted transition, both of which are hindered by electric field, but we have to further explore the tunneling mechanism before concluding the overall effect of electric field.

There is still a lot of future work to do. First, we have to establish a stable solver for Green's tensor in multilayer system, and get the modified energy transfer rate and material gain in several different cavities. Second, we have to find the absorption spectrum modification of Er in electric field, and get the altered energy transfer rate and material gain for our pair of Si-nc and Er in electric field. Meanwhile, we have to investigate the tunneling mechanism, its effect on our system, and the stability and efficiency of electrical pumping. When these are done, we can explore the silicon laser settings involving both microcavity and electric field. Up to now, we are still confined in a single pair of Si-nc and Er.

The next step is the collective effects. In reality, Er doped Si-nc samples contain a distribution of Si-nc's randomly dispersed within SiO_2 matrix. The goal of this part of the research is to apply the developments in a single pair of Si-nc and Er to such cases. For this two major studies need to be done:

1. Energy relaxation via Forster transfer:

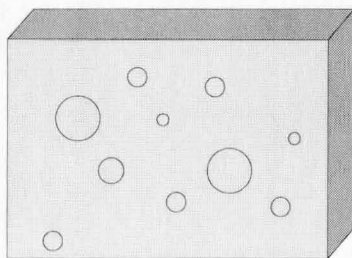

Figure 5-1 Random distribution of Si- nc's in SiO_2 matrix.

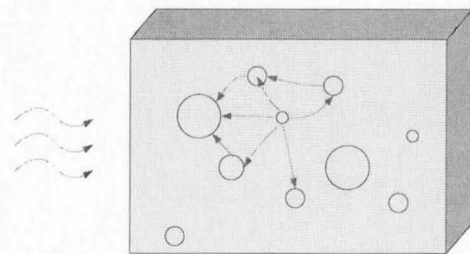

Figure 5-2 Forster energy transfer between different Si-nc's.

We consider a distribution of Si-nc's in SiO_2 with given size distributions and densities (Figure 5-1). The idea is to address the issue of how energies of optically or electrically pumped Si-nc's can transfer from smaller nc to larger nc (Figure 5-2). One direct implication of this study would be calculation of emission spectrum of the Si-nc sample when it is exposed to a laser field.

2. Forster energy transfer in Er-doped Si-nc systems:

Based on the above-mentioned studies, we can move forward to the calculation of gain in Er-doped Si-nc system including the realistic distribution of both Si-nc's and Er ions (Figure 5-3).

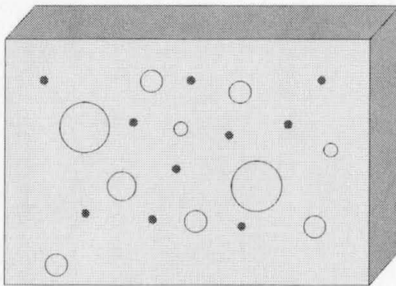

Figure 5-3 Random distribution of Si-nc's and Er.

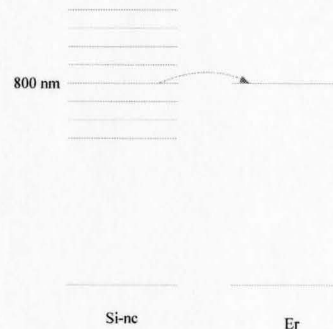

Figure 5-4 Inhomogeneous broadening of Si-nc's.

The distribution of Si-nc's provides the inhomogeneous broadening of states to each Er ions (Figure 5-4). We shall find the gain associated with Er ions and how the electric field influences this.

The above studies can be used for various device applications, including silicon based lasers and amplifiers. We have to simulate the actual structure designs along with the material properties. This should give us a design kit for silicon laser and amplifier.

References

[1] Lorenzo Pavesi, "Routes toward silicon-based lasers", *Materialstoday*, pp.18, January 2005.

[2] Salvatore Coffa, "Light from silicon", *IEEE Spectrum*, pp. 44, Oct. 2005.

[3] D. E. Blakie, "Coupled luminescence centres in erbium-doped silicon rich silicon oxide thin films deposited by ECR-PECVD", M.A.Sc. thesis, McMaster University, 2006.

[4] Martin A. Green, Jianhua Zhao, Aihua Wang, Peter J. Reece, Michael Gal, "Efficient silicon light-emitting diodes", *Nature* **412**, 805 (2001).

[5] Wai Lek Ng, M. A. Lourenço, R. M. Gwilliam, S. Ledain, G. Shao, K. P. Homewood, "An efficient room-temperature silicon-based light-emitting diode", *Nature* **410**, 192 (2001).

[6] T. Stoica, L. Vescan, A. Mück, B. Holländer and G. Schöpe, "Electroluminescence study on electron hole plasma in strained SiGe epitaxial layers", *Physica E* **16**, 359 (2003).

[7] F. Iacona, G. Franzo and C. Spinella, "Correlation between luminescence and structural properties of Si nanocrystals", *J. Appl. Phys.* **87**, 1295 (2000).

[8] G. Franzo, D. Pacifica, V. Vinciguerra, F. Priolo and F. Iacona, "Er3+ ions-Si nanocrystals interactions and their effects on the luminescence properties", *Appl. Phys. Lett.* **76**, 2167 (2000).

[9] Haisheng Rong, Richard Jones, Ansheng Liu, Oded Cohen, Dani Hak, Alexander Fang, Mario Paniccia, "A continuous-wave Raman silicon laser", *Nature* **433**, 725 (2005).

[10] Alexander W. Fang, Hyundai Park, Oded Cohen, Richard Jones, Mario J. Paniccia, and John E. Bowers, "Electrically pumped hybrid AlGaInAs-silicon evanescent laser", *Optics Express* **14**, 9203 (2006).

[11] Lukas Novotny and Bert Hecht, *Principles of nano-optics*, Chapter 8, Cambridge University Press, 2006.

[12] Hideki Fujiwara, Keiji Sasaki, and Hiroshi Masuhara, "Enhancement of Forster Energy Transfer within a Microspherical Cavity", *ChemPhysChem* **6**, 2410 (2005).

[13] Govind P. Agrawal, *Fiber-optic communication systems*, 2nd Ed., John Wiley & Sons, Inc. , 1997.

[14] Fabio Iacona, Giorgia Franzò, Eduardo Ceretta Moreira, and Francesco Priolo, "Silicon nanocrystals and Er3+ ions in an optical microcavity", *J. Appl. Phys.* **89**, 8354 (2001).

[15] Carl B. Poitras, "Light emitting materials and control of their emission properties for applications in integrated optics", Ph.D. thesis, Cornell University, 2006.

[16] Vilson R. Almeida, Qianfan Xu, Carlos A. Barrios, and Michal Lipson, "Guiding and confining light in void nanostructure", *Opt. Lett.* **29**, 1209 (2004).

[17] Carlos Angulo Barrios, Michal Lipson, "Electrically driven silicon resonant light emitting device based on slot-waveguide", *Optics Express* **13**, 10092 (2005).

[18] O. Painter, R. K. Lee, A. Scherer, A. Yariv, J. D. O'Brien, P. D. Dapkus, and I. Kim, "Two-dimensional photonic band-gap defect mode laser", *Science* **284**, 1819 (1999).

[19] Domenico Pacifici, Giorgia Franzo, Francesco Priolo, Fabio Iacona, and Luca Dal Negro, "Modeling and perspectives of the Si nanocrystals–Er interaction for optical amplification", *Phys. Rev. B* **67**, 245301 (2003).

[20] Hansuek Lee, Jung Shin, and Namkyoo Park, "Performance analysis of nanocluster-Si sensitized Er-doped waveguide amplifier using top-pumped 470nm LED", *Optics Express* **13**, 9881 (2005).

[21] Gunnar Bjork , "On the spontaneous lifetime change in an ideal planar microcavity-transition from a mode continuum to quantized modes", *IEEE J. Quan. Electron.* **30**, 2314 (1994).

[22] C. Randy Giles and Emmanuel Desurvire, "Modeling erbium-doped fiber amplifiers", *J. Lightwave Tech.* **9**, 271 (1991).

[23] Satoru Miura, Toshihiro Nakamura, Minoru Fujii, Masaki Inui, and Shinji Hayashi, "Size dependence of photoluminescence quantum efficiency of Si nanocrystals", *Phys. Rev. B* **73**, 245333 (2006).

[24] R. L. Hartman, S. M. Cohen, and P. T. Leung, "A note on the green dyadic calculation of the decay rates for admolecules at multiple planar interfaces", *J. Chem. Phys.* **110**, 2189 (1999).

[25] Robert L. Hartman, "Green dyadic calculations for inhomogeneous optical media", *J. Opt. Soc. Am. A* **17**, 1067 (2000).

[26] Michael Paulus, Phillipe Gay-Balmaz, and Olivier J. F. Martin, "Accurate and efficient computation of the Green's tensor for stratified media", *Phys. Rev. E* **62**, 5797 (2000).

[27] Krzysztof A. Michalski, "Extrapolation methods for Sommerfeld integral tails", *IEEE Tran. Antennas and Propagation* **46**, 1504 (1998).

[28] Maria Eloisa Castagna, Salvatore Coffa, Mariantonietta Monaco, Anna Muscara, Liliana Caristia, Simona Lorenti and Alberto Messina, "High efficiency light emitting devices in silicon", *Mater. Sci. Eng. B* **105**, 83 (2003).

[29] Anna Muscará, Maria Eloisa Castagna, Salvatore Leonardi, Salvatore Coffa, Liliana Caristia and Simona Lorenti, "Design and electro-optical characterization of Si-based resonant cavity light emitting devices at 850 nm", *J. Luminescence* **121**, 293 (2006).

[30] David J. Griffiths, *Introduction to Quantum Mechanics*, 2nd Ed., Pearson, 2005.

[31] Rolf. Enderlein, Norman J. M. Horing, *Fundamentals of Semiconductor Physics and Devices*, World Scientific, 1997.

[32] T. Ouisse and A. G. Nassiopoulou, "Dependence of the radiative recombination lifetime upon electric field in silicon quantum dots embedded into SiO_2", *Europhys. Lett.* **51**, 168 (2000).

[33] Mark S. Hybertsen, "Absorption and emission of light in nanoscale silicon structures", *Phys. Rev. Lett.* **72**, 1514 (1994).